Journal of Advanced Ceramics
2023, **12**(5): 954–971
https://doi.org/10.26599/JAC.2023.9220731
ISSN 2226-4108
CN 10-1154/TQ

Research Article

Rare-earth and transition metal ion single-/co-doped double-perovskite tantalate phosphors: Validation of suitability for versatile applications

Yongbin Hua[a], Jae Su Yu[a,*], Li Li[b,*]

[a]*Department of Electronics and Information Convergence Engineering, Institute for Wearable Convergence Electronics, Kyung Hee University, Yongin-si 17104, Republic of Korea*
[b]*School of Science, Chongqing University of Posts and Telecommunications, Chongqing 400065, China*

Received: November 24, 2022; Revised: February 7, 2023; Accepted: February 12, 2023

Abstract: Novel rare-earth (RE; e.g., europium (Eu^{3+}), samarium (Sm^{3+}), and praseodymium (Pr^{3+})) and transition metal (TM^{4+}; e.g., manganese (Mn^{4+})) ion single-/co-doped double-perovskite Ca_2InTaO_6 (CITO) phosphors were prepared and investigated with respect to their crystal structure and photoluminescence (PL) properties. Among them, the CITO:Eu^{3+} phosphors were found to exhibit an ultra-high internal PL quantum yield (89.1%) and good thermal stability (78.7% at 423 K relative to the initial value at 303 K). As such, the corresponding packaged white light-emitting diode (LED) was able to display a remarkable color rendering index (CRI; = 91.51@10 mA). Besides, the potential in applications of anti-counterfeiting fields and a novel LED structure based on flexible phosphor-converted films was also studied. Moreover, due to their different thermal quenching, trivalent lanthanide (Ln^{3+})/Mn^{4+} co-doped CITO phosphors were designed for optical thermometry based on the luminescence intensity ratio (LIR) between different 4f transitions of various Ln^{3+} ions and $^2E_g \rightarrow {}^4A_{2g}$ (Mn^{4+}) transition. Particularly, the LIR between the $^4G_{5/2} \rightarrow {}^6H_{9/2}$ and $^2E_g \rightarrow {}^4A_{2g}$ peaks of the CITO activated with 5 mol% Sm^{3+} and 0.3 mol% Mn^{4+} exhibited the most excellent relative sensitivity (S_r; = 3.80 %·K^{-1}) with beneficial temperature uncertainty of 0.0648 K. Overall, these results are of significance to offer valuable databases for constructing multifunctional high-performance optical platforms using single-/co-doped double-perovskite tantalates.

Keywords: phosphors; quantum yields (QYs); light-emitting diodes (LEDs); thermometry; anti-counterfeiting

1 Introduction

In recent decades, trivalent lanthanides (Ln^{3+}; e.g., europium (Eu^{3+}), samarium (Sm^{3+}), and praseodymium (Pr^{3+})) and tetravalent transition metal (TM^{4+}; e.g. manganese (Mn^{4+})) ion-activated phosphors have been widely utilized in various applications because of their beneficial optical properties. Although the most commonly used artificial solid-state white light source is the white light-emitting diode (LED) fabricated by yellow-emitting $Y_3Al_5O_{12}$:Ce^{3+} (YAG:Ce^{3+}) phosphors onto a blue GaN chip, Refs. [1–5] confirm that the white LED based on the YAG:Ce^{3+} phosphors suffers from various drawbacks such as low color rendering index (CRI; < 80) and high correlated color temperature (CCT; > 5000 K) as a result of lacking a red-emitting

* Corresponding authors.
E-mail: J. S. Yu, jsyu@khu.ac.kr;
L. Li, lilic@cqupt.edu.cn

region. Fortunately, the combination of mixed red–green–blue (RGB) phosphors and near-ultraviolet (NUV)/ultraviolet (UV) LED chips can improve the quality of white LED devices due to their achievement of an ideal white glow. Some researchers [6–9] considered that the limited light efficiency and high cost of the RGB phosphors will restrict the sustainable development of the white LED devices, so they still focus on the color quality enhancement of the white LED based on the yellow phosphors and blue chips. Note that most researchers will use red-emitting phosphors. As such, the good performance of red-emitting phosphors plays a vital role in the quality enhancement of the white LED devices. The Eu^{3+}-doped red-emitting phosphors with abundant transitions from the excited $^5D_0$ level to the ^7F_J (J = 0, 1, 2, 3, and 4) levels of the $4f_6$ electron configuration can obtain high photoluminescence (PL) quantum yield (PLQY) for the white LED devices with high CRI, such as $Cs_3GdGe_3O_9$:Eu^{3+} and $BaZrGe_3O_9$:Eu^{3+} phosphors [10,11] wherein ^7F_J (J = 0, 1, 2, 3, and 4) stands for the specific spectral terms of Eu^{3+} ions. In addition, orange-reddish-emitting Sm^{3+}-activated phosphors (e.g., $CaSc_2O_4$:Sm^{3+} and Ca_2InSbO_6:Sm^{3+} phosphors) with the unique $^4G_{5/2} \rightarrow {}^6H_J$ (J = 5/2, 7/2, 9/2, and 11/2) transitions can offer good thermal stability for the white LED devices [12,13]. Meanwhile, Mn^{4+}-doped materials with a specific $3d^3$ electron structure can exhibit strong deep- red emission, which has been also determined as a kind of candidate for preparing the white LED devices [14–17].

Moreover, Ln^{3+} (e.g., Eu^{3+}, Sm^{3+}, and Pr^{3+}) and Mn^{4+} single-/co-doped phosphors have been applied in other fields including solar cells, drug delivery, field emission displays, lasers, anti-counterfeiting films, batteries, luminescence intensity ratio (LIR) thermometry, luminescence lifetime thermometry, and pressure-dependent manometry [18–30]. Ca_2InTaO_6 (CITO) with a double-perovskite ($A_2BB'O_6$) structure provided highly distorted [InO_6] octahedron for Ln^{3+} and [TaO_6] octahedron for Mn^{4+}, which can lead to good luminescence performance. However, the systematic investigations of the Eu^{3+}, Sm^{3+}, Pr^{3+}, and Mn^{4+} single-/co-doped CITO phosphors are rarely reported. Hence, in this work, the Eu^{3+}, Sm^{3+}, Pr^{3+}, and Mn^{4+} single-/co-doped CITO phosphors were prepared and further studied in terms of their structure and optical properties (e.g., phase structure, concentration quenching mechanism, thermal stability, and QY). In this regard, the optimized CITO:Eu^{3+} phosphors exhibited an ultra-high internal PLQY, and its packaged white LED device provided an excellent CRI value. In addition, a novel alternative anti-counterfeiting strategy based on the flexible phosphor-converted polydimethylsiloxane light-emitting films with good anti-stress and humidity properties was introduced. Such strategy was confirmed with many advantages (e.g., simple operation and recyclability) relative to phosphor-based security inks [31–33]. Owing to different thermal quenching (thermal quenching efficiency at various temperatures) of the CITO:Eu^{3+}, CITO:Sm^{3+}, CITO:Pr^{3+}, and CITO:Mn^{4+} phosphors, the Ln^{3+}/Mn^{4+} co-doped phosphors were prepared for potential temperature-dependent LIR thermometry. Interestingly, the sensing sensitivity of the LIR thermometry would be greatly affected by different transition peaks and doping ions. Among them, the CITO:Sm^{3+}/Mn^{4+} phosphors displayed the highest relative sensitivity (S_r).

2 Experimental

The starting materials including $CaCO_3$ (≥ 99.0%), In_2O_3 (99.99%), Ta_2O_5 (99%), Eu_2O_3 (99.9%), $Sm(NO_3)_3·6H_2O$ (99.9%), $Pr(NO_3)_3·6H_2O$ (99.9%), and $MnCO_3$ (≥ 99.9%) materials were ordered from Sigma-Aldrich Co., Ltd. These raw materials were stoichiometrically weighed based on the formulae of $Ca_2In_{1-x_1}TaO_6$:x_1Eu^{3+} (CITO:Eu^{3+}; x_1 = 10, 20, 30, 40, 50, and 60 mol%), $Ca_2In_{1-x_2}TaO_6$:x_2Sm^{3+} (CITO:Sm^{3+}; x_2 = 1, 5, 10, 15, and 20 mol%), $Ca_2In_{1-x_3}TaO_6$:x_3Pr^{3+} (CITO:Pr^{3+}; x_3 = 1, 5, 10, 15, and 20 mol%), and $Ca_2InTa_{1-x_4}O_6$:x_4Mn^{4+} (CITO:Mn^{4+}; x_4 = 0.1, 0.3, 0.6, 0.9, and 1.2 mol%). Next, the mixed powders were ground for 30 min and further sintered at the temperature of 1400 ℃ (5 ℃/min) for 5 h. The co-doped phosphors including $Ca_2In_{0.6}Ta_{0.997}O_6$:0.4$Eu^{3+}$/0.003$Mn^{4+}$, $Ca_2In_{0.95}Ta_{0.997}O_6$:0.05$Sm^{3+}$/0.003$Mn^{4+}$, and $Ca_2In_{0.95}Ta_{0.997}O_6$:0.05$Pr^{3+}$/0.003$Mn^{4+}$ phosphors were prepared by the above-mentioned same processes and noted as CITO:0.4Eu^{3+}/0.003Mn^{4+}, CITO:0.05Sm^{3+}/0.003Mn^{4+}, and CITO:0.05Pr^{3+}/0.003Mn^{4+}, respectively.

X-ray diffraction (XRD) patterns were detected by an X-ray diffractometer (D8 Advance, Bruker; Cu Kα1, wavelength (λ) = 0.15406 nm) with a scan rate of 3 (°)/min. A field-emission scanning electron microscope (FE-SEM; LEO SUPRA 55, Carl Zeiss) was utilized to analyze morphology and energy-dispersive X-ray

spectroscopy (EDS) patterns. Rietveld refinements and crystal structures were presented with the aid of the General Structure Analysis System (GSAS) software and VESTA 2.0 software. A fluorescence spectrophotometer (FluroMate FS-2, SCINCO) with a heating platform was employed to record PL excitation (PLE) and PL emission spectra. The internal PLQY was determined by Quantaurus-QY Plus (Hamamatsu Photonics). Decay curves were measured by a fluorimeter (QuantaMaster 8000, Photon Technology International (PTI)). The packaged LED devices were measured by adopting a multi-channel spectroradiometer (OL770, G&H).

As for the white LED device, a certain amount of the optimal CITO:Eu^{4+} (40 mol% of Eu^{3+}) and commercial phosphors of green-emitting $(Ba,Sr)_2SiO_4$:Eu^{2+} (BSS:Eu^{2+}) and blue-emitting $BaMgAl_{10}O_{17}$:Eu^{2+} (BAM:Eu^{2+}) were mixed with gel A and gel B (A : B = 1 g : 1 g). Then, the mixed slurry was dripped onto the LED chips (~385 and ~405 nm) and further dried in an oven at a temperature of 80 ℃ for 2 h. CITO:Eu^{3+} and CITO:Pr^{3+} phosphor-converted films were fabricated by mixing the optimal doping sample of 0.3 g into base resin of 2.5 g and curing agent of 0.25 g (Sylgard 184, Dow Corning Co., Ltd.). Afterward, the mixed slurry was vacuumed and dried in an oven at 70 ℃ for 2 h. Similarly, CITO:Pr^{3+}–BAM:Eu^{2+} films were made of 0.5 g CITO:0.05Pr^{3+}, 0.05 g BAM:Eu^{2+}, 3 g base resin, and 0.3 g curing agent; afterward, the above-mixed slurry was poured into a mold and dried eventually. The red-emitting LED device based on the phosphor-converted film was fabricated by the red-emitting CITO:Eu^{3+} film in a circle with a diameter of 1 cm to cover the ~385 nm LED chip, while the mixed AB gel (gel A : gel B = 1 : 1) was used as adhesive materials.

3 Results and discussion

The recorded diffraction peaks of the obtained single-/co-doped samples can be perfectly indexed to the Ca_2InNbO_6 (ICSD Card No. 99697), revealing that the luminescent activator-doped CITO materials have the *P*21/*n* (14) space group in monoclinic phase, as shown in Fig. 1(a). Also, the luminescent activators can be substituted for the cation sites, which slightly affects the crystal structure. In the CITO lattice, Ca at the 4*e* site connects three oxygen atoms, while In at the 2*a* site and Ta at the 2*b* site are surrounded by six oxygen atoms to form octahedrons of [InO_6] and [TaO_6], as shown in Fig. 1(b). It is well-known that rare-earth (RE) ions are likely to occupy the In^{3+} sites in the CITO lattice for maintaining the conservation of chemical valence according to Refs. [34,35]. On the other hand, the [TaO_6] octahedron at the 2*b* site can provide good environment for the splitting of the crystal field of the $3d^3$ states of Mn^{4+} to result in strong emission intensity. Of course, the materials doped with low concentrations can create oxygen vacancies for compensating valence loss. Therefore, Mn^{4+} has been promised to take the place of the $B'^{(+5)}$ site in $A_2BB'O_6$ typed double-perovskites [36–38]. On the other hand, similar ionic radii are also used to identify the possibility of forming a new solid-state solution by calculating the radius percentage difference (D_r) [39,40]. In this work, when the coordinate number is determined to be 6, the radii of the In^{3+}, Ta^{5+}, Eu^{3+}, Sm^{3+}, Pr^{3+}, and Mn^{4+} are 0.8, 0.64, 0.947, 0.958, 0.99, and 0.53 Å, respectively. Thereby, D_r of the Eu^{3+}–In^{3+}, Sm^{3+}–In^{3+}, Pr^{3+}–In^{3+}, and Mn^{4+}–Ta^{5+} combinations were determined to be about −18.38%, −19.75%, −23.75%, and 17.19%, respectively. Obviously, the small calculated D_r (< 30%) demonstrated that the RE^{3+} ion would substitute the In^{3+} site when the Mn^{4+} ion occupied the Ta^{5+} site, as shown in the inset of Fig. 1(b). For an in-depth study of their crystal structure information (e.g., lattice parameters, fractional coordinates, and specific occupied positions), the Rietveld refinements of the CITO:0.4Eu^{3+}/0.003Mn^{4+}, CITO:0.05Sm^{3+}/0.003Mn^{4+}, and CITO:0.05Pr^{3+}/0.003Mn^{4+} phosphors are presented in Figs. 1(c)–1(e). Note that their small fitting factors (wR_p and R_p where wR_p is the weighted profile factor, and R_p is the profile factor) indicate that their refinement results are quite reasonable and convincing. As listed in Table 1, the lattice parameters (*a*, *b*, *c*, *α*, *β*, and *γ*) and volume (*V*) of the co-doped samples were provided. Particularly, the *V* values of the CITO:0.4Eu^{3+}/0.003Mn^{4+}, CITO:0.05Sm^{3+}/0.003Mn^{4+}, and CITO:0.05Pr^{3+}/0.003Mn^{4+} phosphors were calculated to be about 256.7592, 253.0285, and 253.2471 $Å^3$, respectively. In spite of the Eu^{3+} ion having the smallest radius in relation to the Sm^{3+} and Pr^{3+} ions, the larger doping content of Eu^{3+} (40 mol%) is the dominant factor to obtain the largest *V* after substituting the In^{3+} ion with a smaller radius. Under the same doping content of 5 mol% RE^{3+}, *V* of the CITO:0.05Pr^{3+}/0.003Mn^{4+} phosphor is a little larger than that of the CITO:0.05Sm^{3+}/0.003Mn^{4+} phosphor, which is well consistent with the previous results that the radius of Pr^{3+} is larger than that of Sm^{3+}.

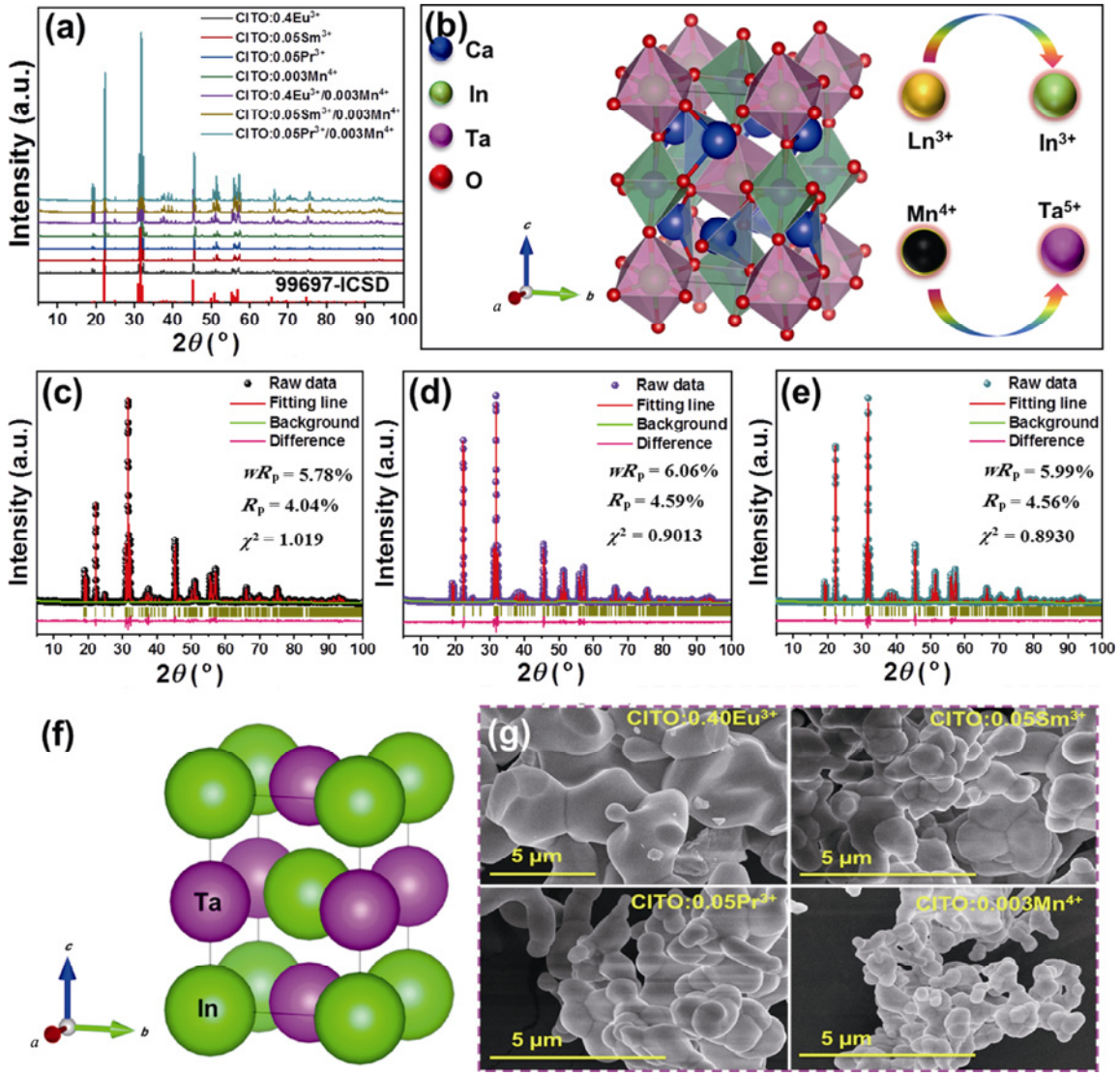

Fig. 1 (a) XRD patterns of obtained samples. (b) Simplified crystal structure of CITO host lattice. Rietveld refinements of (c) CITO:0.4Eu^{3+}/0.003Mn^{4+}, (d) CITO:0.05Sm^{3+}/0.003Mn^{4+}, and (e) CITO:0.05Pr^{3+}/0.003Mn^{4+} phosphors. (f) Main bracket of CITO unit cell. (g) FE-SEM images of the CITO:0.4Eu^{3+}, CITO:0.05Sm^{3+}, CITO:0.05Pr^{3+}, and CITO:0.003Mn^{4+} phosphors.

Table 1 Rietveld XRD refinements of luminescent activator co-doped samples

	CITO:0.4Eu^{3+}/0.003Mn^{4+}	CITO:0.05Sm^{3+}/0.003Mn^{4+}	CITO:0.05Pr^{3+}/0.003Mn^{4+}
Radiation	Cu Kα1 radiation	Cu Kα1 radiation	Cu Kα1 radiation
2θ range (°)	5–100	5–100	5–100
Structure	Monoclinic ($P21/n$ (14))	Monoclinic ($P21/n$ (14))	Monoclinic ($P21/n$ (14))
Lattice parameter and V	a = 5.5596 Å	a = 5.5476 Å	a = 5.5504 Å
	b = 5.7749 Å	b = 5.7319 Å	b = 5.7323 Å
	c = 7.9972 Å	c = 7.9573 Å	c = 7.9596 Å
	α = 90.0000°	α = 90.0000°	α = 90.0000°
	β = 90.1400°	β = 89.9225°	β = 89.9077°
	γ = 90.0000°	γ = 90.0000°	γ = 90.0000°
	$V \approx$ 256.7592 Å^3	$V \approx$ 253.0285 Å^3	$V \approx$ 253.2471 Å^3

Besides, the structural distortion (t) of the luminescent activator co-doped samples in double-perovskite materials can be evaluated as [41,42]:

$$t = \frac{r_A + r_O}{\sqrt{2}\left(\frac{r_B}{2} + \frac{r_{B'}}{2} + r_O\right)} \quad (1)$$

where r_A is the cation radius at the A site in $A_2BB'O_6$ double-perovskite, r_B is the cation radius at the B site in $A_2BB'O_6$ double-perovskite, $r_{B'}$ is the cation radius at the B' site in $A_2BB'O_6$ double-perovskite, and r_O is the radius of the oxygen ion. In this work, the RE^{3+} and Mn^{4+} ions substituted the B and B' sites, respectively. Thus, the t value can be obtained by Eq. (2):

$$t = \frac{r_A + r_O}{\sqrt{2}\left[\frac{(1-x)r_B + xr_{B_1}}{2} + \frac{(1-y)r_{B'} + yr_{B'_1}}{2} + r_O\right]} \quad (2)$$

where xr_{B1} is the cation radius at the B site of the doping ion, and $yr_{B'1}$ is the cation radius at the B' site of the doping ion. As for the co-doped samples, the t values were calculated by Eqs. (3)–(5):

$$t_{Eu-Mn} = \frac{r_{Ca} + r_O}{\sqrt{2}\left(\frac{0.6r_{In} + 0.4r_{Eu}}{2} + \frac{0.997r_{Ta} + 0.003r_{Mn}}{2} + r_O\right)} \quad (3)$$

$$t_{Sm-Mn} = \frac{r_{Ca} + r_O}{\sqrt{2}\left(\frac{0.95r_{In} + 0.05r_{Sm}}{2} + \frac{0.997r_{Ta} + 0.003r_{Mn}}{2} + r_O\right)} \quad (4)$$

$$t_{Pr-Mn} = \frac{r_{Ca} + r_O}{\sqrt{2}\left(\frac{0.95r_{In} + 0.05r_{Pr}}{2} + \frac{0.997r_{Ta} + 0.003r_{Mn}}{2} + r_O\right)} \quad (5)$$

where t_{Eu-Mn} is the structural distortion of Eu^{3+}/Mn^{4+} co-doped CITO host, t_{Sm-Mn} is the structural distortion of Sm^{3+}/Mn^{4+} co-doped CITO host, and t_{Pr-Mn} is the structural distortion of Pr^{3+}/Mn^{4+} co-doped CITO host. Here, r_{Ca} is the radius of Ca^{2+}, r_{In} is the radius of In^{3+}, r_{Eu} is the radius of Eu^{3+}, r_{Ta} is the radius of Ta^{5+}, r_{Mn} is the radius of Mn^{4+}, r_{Sm} is the radius of Sm^{3+}, and r_{Pr} is the radius of Pr^{3+}. Hence, the t values were calculated to be about 0.78961, 0.79907, and 0.79877 for the CITO:0.4Eu^{3+}/ 0.003Mn^{4+}, CITO:0.05Sm^{3+}/0.003Mn^{4+}, and CITO:0.05Pr^{3+}/ 0.003Mn^{4+} phosphors, respectively. Due to 0.78961 < 0.79877 < 0.79907 < "1", it is suggested that the CITO:0.4Eu^{3+}/0.003Mn^{4+} phosphor has the most high-degree t, while the CITO:0.05Pr^{3+}/0.003Mn^{4+} and CITO:0.05Sm^{3+}/0.003Mn^{4+} phosphors in turns. It is noted that the calculated t values can be in line with the results of the Rietveld XRD refinements. Clearly, the β angles (initial value: 90.0000°) of the CITO:0.4Eu^{3+}/ 0.003Mn^{4+}, CITO:0.05Sm^{3+}/0.003Mn^{4+}, and CITO:0.05Pr^{3+}/ 0.003Mn^{4+} phosphors were 90.1400° (difference: 0.1400°), 89.9225° (difference: 0.0775°), and 89.9077° (difference: 0.0923°), respectively. Since the radii of different doping ions and substituted cations are different, the above-mentioned way will affect the length of a covalent bond as well as slight t, thereby resulting in the change of fractional coordinates, as listed in Table 2. Interestingly, the In and Ta sites are the main bracket of a CITO unit cell, as shown in Fig. 1(f).

The In at the 2*a* site and Ta at the 2*b* site formed a basic structure of the CITO lattice. This means that the crystal structure of the CITO is composed of abundant octahedrons of [InO_6] and [TaO_6] to form a skeleton, while Ca at the 4*e* site fills the center of octahedral cavities, which is the main reason why the fractional coordinates did not change after doping the luminescent activators. Figure 1(g) shows typical FE-SEM images of the Ln^{3+} and Mn^{4+} single-doped materials. Indisputably, the obtained samples were highly aggregated and irregularly shaped due to long-time calcination at high temperatures. It is worth noting that the particle size of

Table 2 Fractional coordinates of co-doped samples

Sample	Name	Fractional coordinate			Site
CITO:0.4Eu^{3+}/ 0.003Mn^{4+}	Ca	0.490158	−0.055619	0.255192	4*e*
	In/Eu	0.000000	0.000000	0.000000	2*a*
	Ta/Mn	0.000000	0.000000	0.500000	2*b*
	O(1)	0.313088	0.807468	0.936875	4*e*
	O(2)	0.198875	0.299844	0.938583	4*e*
	O(3)	0.109957	0.043604	0.257094	4*e*
CITO:0.05Sm^{3+}/ 0.003Mn^{4+}	Ca	0.518669	−0.059376	0.258348	4e
	In/Eu	0.000000	0.000000	0.000000	2a
	Ta/Mn	0.000000	0.000000	0.500000	2b
	O(1)	0.329799	0.787785	0.947115	4e
	O(2)	0.217124	0.309791	0.941128	4e
	O(3)	0.115483	0.032295	0.245014	4e
CITO:0.05Pr^{3+}/ 0.003Mn^{4+}	Ca	0.519896	−0.053364	0.252512	4e
	In/Eu	0.000000	0.000000	0.000000	2a
	Ta/Mn	0.000000	0.000000	0.500000	2b
	O(1)	0.315842	0.783506	0.942549	4e
	O(2)	0.205211	0.316280	0.944483	4e
	O(3)	0.107739	0.042657	0.258505	4e

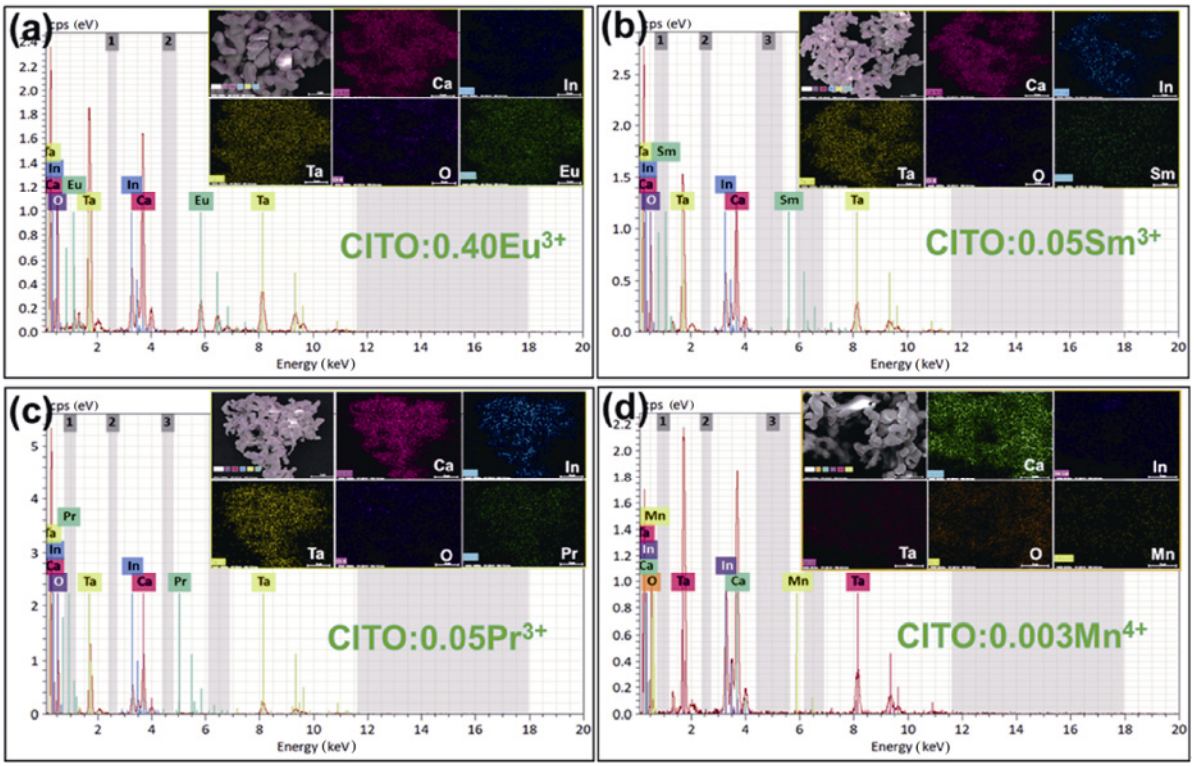

Fig. 2 EDS spectra of (a) CITO:0.4Eu^{3+}, (b) CITO:0.05Sm^{3+}, (c) CITO:0.05Pr^{3+}, and (d) CITO:0.003Mn^{4+} phosphors. The insets of (a–d) show their corresponding elemental mapping images.

the CITO:0.4Eu^{3+} phosphor was the largest, while that of the CITO:0.003Mn^{4+} phosphor appeared to be relatively small. As displayed in Figs. 2(a)–2(d), the EDS spectra identified that these fundamental elements can be accurately detected as well as evenly distributed over the particle surface. In light of the above evidence, the luminescent activators of the Ln^{3+} and Mn^{4+} ions have been successfully incorporated into the CITO lattice.

Under the emission wavelength (λ_{em}) of 618 nm, the PLE spectra in the wavelength range of 200–500 nm consisted of the charge transfer band (CTB) and the peaks corresponding to the $^7F_0 \rightarrow (^5D_4, ^5L_7, ^5L_6, ^5D_3,$ and $^5D_2)$ transitions, while the strongest peak was related to the $^7F_0 \rightarrow {}^5L_6$ transition, locating at around 396 nm for the CITO:Eu^{3+} phosphors, as displayed in Fig. 3(a). Afterward, the PL emission including the magnetic-dipole $^5D_0 \rightarrow {}^7F_1$ (593 nm), electric-dipole $^5D_0 \rightarrow {}^7F_2$ (618 nm) and $^5D_0 \rightarrow {}^7F_4$ (704 nm), and forbidden $^5D_0 \rightarrow {}^7F_3$ (656 nm) transitions were recorded under the excitation wavelength (λ_{ex}) of 396 nm, as illustrated in Fig. 3(b). Owing to the admixture of odd-parity electronic configuration to the pure 4f transitions, the dominated emission peak of the CITO:Eu^{3+} phosphors was assigned to the $^5D_0 \rightarrow {}^7F_2$ transition, and the optimal doping concentration was found to be 40 mol%, as shown in the inset of Fig. 3(b). The emergence of concentration quenching leads to a decrease in the emission intensity with a continued increase in the doping concentration because the non-radiative transition rate saturates. According to the previous literature, the concentration quenching mechanism can be determined by Blasse's and Dexter's theory [43–45]. Figure 3(c) displays a plot of log$x$ vs. log(I/x) for the CITO:Eu^{3+} phosphors where I is the PL emission intensity. The interaction coefficient (Q) value was estimated to be ~5.42 (close to 6), implying that the dipole–dipole interaction (Q = 6) was the main route to control the concentration quenching mechanism of the CITO:Eu^{3+} phosphors rather than the dipole–quadrupole (Q = 8) and quadrupole–quadrupole (Q = 10) interactions. Figure 3(d) shows the PLE spectra of the CITO:Sm^{3+} phosphors under λ_{em} = 603 nm. Clearly, the PLE spectra included an obvious CTB band originating from the O^{2-}–Sm^{3+} bond and unique Sm^{3+} excitation peaks of the $^6H_{5/2} \rightarrow (^4H_{9/2}, {}^4D_{3/2}, {}^4P_{7/2}, {}^4F_{7/2}, {}^4P_{5/2}, {}^4G_{9/2},$ and $^4I_{9/2})$ transitions. Under the suitable λ_{ex} of 407 nm, the featured $^4G_{5/2} \rightarrow {}^6H_{5/2}$ (magnetic dipole), $^4G_{5/2} \rightarrow {}^6H_{7/2}$ (partially magnetic dipole and partially forced electric dipole), $^4G_{5/2} \rightarrow {}^6H_{9/2}$ (electric dipole), and $^4G_{5/2} \rightarrow {}^6H_{11/2}$

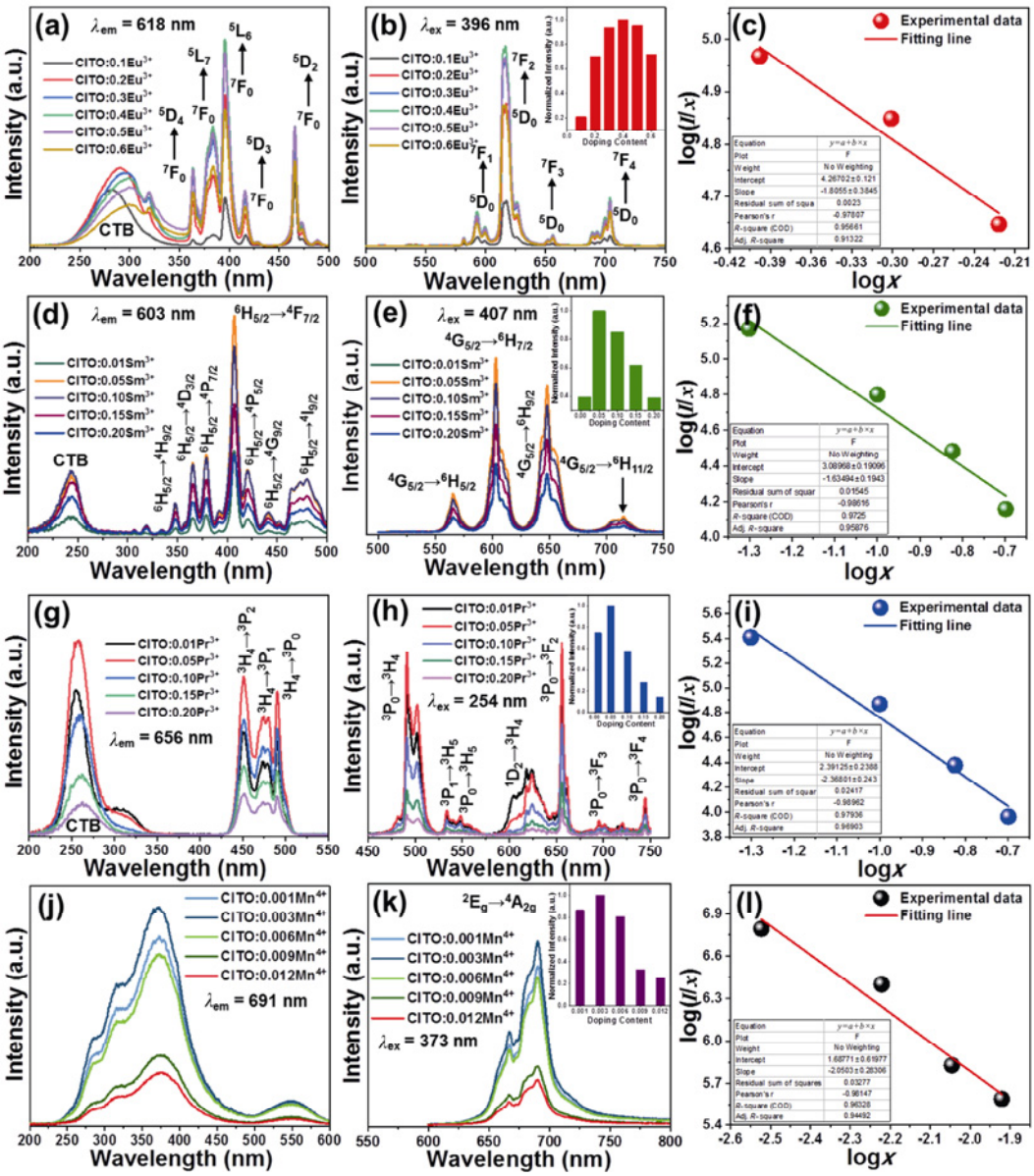

Fig. 3 PLE spectra, PL emission spectra, and plots of log*x* vs. log(*I*/*x*) of (a–c) CITO:Eu^{3+}, (d–f) CITO:Sm^{3+}, (g–i) CITO:Pr^{3+}, and (j–l) CITO:Mn^{4+} phosphors. The insets of (b), (e), (h), and (k) show their corresponding normalized emission intensity values.

(electric dipole) transitions were measured to be located at 566, 603, 648, and 715 nm, respectively. The strongest emission peak is related to the $^4G_{5/2} \rightarrow {}^6H_{7/2}$ transition, as shown in Fig. 3(e). In particular, the optimal doping concentration was 5 mol%, and the possible concentration quenching mechanism was determined to be dipole–dipole interaction because the *Q* value of the CITO:Sm^{3+} phosphors was calculated to be ~4.90, as presented in Fig. 3(f).

The PLE spectra of the CITO:Pr^{3+} phosphors have a strong CTB and several excitation peaks of the $^3H_4 \rightarrow {}^3P_2$, $^3H_4 \rightarrow {}^3P_1$, and $^3H_4 \rightarrow {}^3P_0$ transitions under λ_{em} = 656 nm, as shown in Fig. 3(g). The emission peaks including the $^3P_0 \rightarrow {}^3H_4$ (491 nm, electric dipole), $^3P_1 \rightarrow {}^3H_5$ (534 nm), $^3P_0 \rightarrow {}^3H_5$ (548 nm), $^1D_2 \rightarrow {}^3H_4$ (624 nm), $^3P_0 \rightarrow {}^3F_2$ (656 nm, magnetic dipole), $^3P_0 \rightarrow {}^3F_3$ (695 nm), and $^3P_0 \rightarrow {}^3F_4$ (745 nm) transitions were recorded under λ_{ex} = 254 nm, as presented in Fig. 3(h). Attentively, the $^1D_2$ emission was quenched much faster than the $^3P_0$ emission, which was attributed to the cross-relaxation between $^1D_2 \leftrightarrow {}^1G_4$ and $^3H_4 \leftrightarrow {}^3F_4$ transitions with close energy levels [46]. Since the energy transfer is sensitive to Pr^{3+} ion concentration, the intensity of the fluorescence emitted by $^1D_2$ is strongly concentration-dependent [47]. It should be mentioned that the optimal doping concentration of the

CITO:Pr^{3+} phosphors is similar to that of the CITO:Sm^{3+} phosphors with a value of 5 mol%. Furthermore, the Q value of the CITO:Pr^{3+} phosphors was calculated to be ~7.10 (between 6 and 8), indicating that the concentration quenching might work under the dipole–dipole and dipole–quadrupole interactions, as presented in Fig. 3(i). Eventually, as can be seen in Figs. 3(j) and 3(k), the PLE and PL emission spectra of the CITO:Mn^{4+} phosphors were measured under the λ_{em} and λ_{ex} of 691 and 373 nm, respectively. The CITO:Mn^{4+} phosphors emitted a strong $^2E_g \rightarrow {}^4A_{2g}$ peak under broadband NUV excitation, and 0.3 mol% was further determined as the optimal doping concentration, as shown in the inset of Fig. 3(k). In Fig. 3(l), the Q value was ~6.15, so it is acceptable to consider that the dipole–dipole interaction was most likely to control the concentration quenching in the CITO:Mn^{4+} phosphors. The crystal-field strength (D_q) and nephelauxetic ratio (β_1) can be used to analyze a local structure of Mn^{4+} in the CITO lattice [48,49].

$$D_q = \frac{E(^4A_{2g} \rightarrow {}^4T_{2g})}{10} \tag{6}$$

$$x = \frac{E(^4A_{2g} \rightarrow {}^4T_{1g}) - E(^4A_{2g} \rightarrow {}^4T_{2g})}{D_q} \tag{7}$$

$$\frac{D_q}{B} = \frac{15(x-8)}{x^2 - 10x} \tag{8}$$

$$E(^2E_{2g} \rightarrow {}^4A_{2g})/B = \frac{3.05C}{B} + 7.9 - \frac{1.8B}{D_q} \tag{9}$$

$$\beta_1 = \sqrt{\left(\frac{B}{B_0}\right)^2 + \left(\frac{C}{C_0}\right)^2} \tag{10}$$

As shown in Fig. 4(a), the wavenumbers of band gap transition (valence band–conduction band (VB–CB)), CTB (Mn–O), $^4A_{2g} \rightarrow {}^4T_{1g}$, $^4A_{2g} \rightarrow {}^2T_{2g}$, and $^4A_{2g} \rightarrow {}^4T_{2g}$ transitions were 34,993.1, 31,369.1, 26,949.8, 21,658.3, and 18,312.9 cm^{-1}, respectively. Thus, D_q was 1831.3 cm^{-1} and D_q/B was 1.97, while B was found to be 929.6 cm^{-1} with the help of Eqs. (6)–(8). Racah parameters (B_0 and C_0) of free Mn^{4+} ions were 1160 and 4303 cm^{-1}, respectively. β_1 was calculated to be about 1.01, while C was 2616.2 cm^{-1}. As such, crystal-field strength was not strong in the CITO:Mn^{4+} phosphors due to $D_q/B < 2.3$, as shown in Fig. 4(b). However, it has a strong covalence because $\beta_1 = 1.01 > 1$.

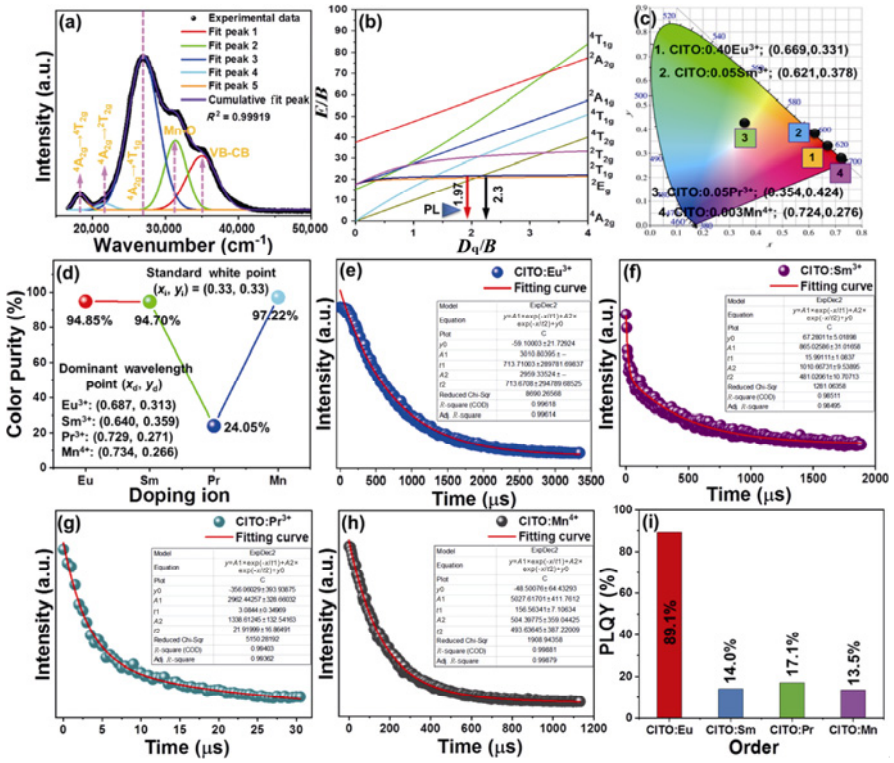

Fig. 4 (a) PLE deconvolution of CITO:0.003Mn^{4+} phosphor. (b) Tanabe–Sugano energy-level diagram for $3d^3$ system in Mn^{4+} octahedral symmetry. (c) Commission Internationale de l'Eclairage (CIE) chromaticity coordinates and (d) color purities of single-doped samples. Decay curves of (e) CITO:0.4Eu^{3+}, (f) CITO:0.05Sm^{3+}, (g) CITO:0.05Pr^{3+}, and (h) CITO:0.003Mn^{4+} phosphors. (i) Internal PLQYs of the prepared phosphors.

CIE chromaticity coordinates of the optimized CITO:0.4Eu^{3+}, CITO:0.05Sm^{3+}, CITO:0.05Pr^{3+}, and CITO:0.003Mn^{4+} phosphors were calculated to be (0.669, 0.331), (0.621, 0.378), (0.354, 0.424), and (0.724, 0.256), respectively. Obviously, due to the unique emission spectra and distinct dominated emission peaks, the CITO:Eu^{3+}, CITO:Sm^{3+}, CITO:Pr^{3+}, and CITO:Mn^{4+} phosphors were located in red, orange, yellow–green, and deep-red regions, respectively, as displayed in Fig. 4(c). Based on the above chromaticity coordinates, their color purities can also be calculated by Eq. (11) [50]:

$$\text{Color purity} = \frac{\sqrt{(x-x_i)^2+(y-y_i)^2}}{\sqrt{(y_d-x_i)^2+(y_d-y_i)^2}} \times 100\% \quad (11)$$

where (x, y), (x_d, y_d), and (x_i, y_i) stand for the chromaticity coordinate of the samples, the dominant wavelength point, and the standard white point, respectively. Consequently, the color purities of the CITO:0.4Eu^{3+}, CITO:0.05Sm^{3+}, CITO:0.05Pr^{3+}, and CITO:0.003Mn^{4+} phosphors were estimated to be 94.85%, 94.70%, 24.05%, and 97.22%, respectively, as shown in Fig. 4(d). The main reason for the low color purity of the CITO:0.05Pr^{3+} phosphor is that scattered emission peaks can be far away from a pure monochromatic region. For the sake of investigating the luminescence dynamic, the decay curves were recorded, as shown in Figs. 4(e)–4(h). It is noted that the decay curve can be well indexed to a double-attenuation model, as given by Eqs. (12) and (13) [51,52]:

$$I = A_1 \exp\left(\frac{-t}{\tau_1}\right) + A_2\left(\frac{-t}{\tau_2}\right) + A_0 \quad (12)$$

$$\tau = \frac{A_1\tau_1^2 + A_2\tau_2^2}{A_1\tau_1 + A_2\tau_2} \quad (13)$$

As a result, the lifetime values of the CITO:0.4Eu^{3+}, CITO:0.05Sm^{3+}, CITO:0.05Pr^{3+}, and CITO:0.003Mn^{4+} phosphors were confirmed to be 713.7, 468.1, 17.4, and 237.6 μs, respectively. In the meantime, the internal PLQY was identified by the third-party international certification institute (KOLAS International Accredited Testing and Certification Agency, Kyung Hee University Industry-University Cooperation Foundation, Core Facility Center (Analysis of Optoelectronic Materials and Devices)). Remarkably, the internal PLQY of the CITO:0.4Eu^{3+} phosphor reached 89.1%, which is much higher than those of CITO:0.05Sm^{3+} (14.0%), CITO:0.05Pr^{3+} (17.1%), and CITO:0.003Mn^{4+} (13.5%) phosphors, as shown in Fig. 4(i) and Figs. S1–S4 in the Electronic Supplementary Material (ESM).

Figures 5(a)–5(d) show three-dimensional (3D) and two-dimensional (2D) fluorescence topographical mappings of the CITO:0.4Eu^{3+}, CITO:0.05Sm^{3+}, CITO:0.05Pr^{3+}, and CITO:0.003Mn^{4+} phosphors. Evidently, the PL emission intensity gradually decreased with the increase in the temperature as a result of thermal quenching. In general, the remained intensity at 423 K needs to be compared with respect to their initial intensity because the temperature of conventional lighting devices can reach 423 K in real-world applications. In this study, the emission intensity values of the CITO:0.4Eu^{3+}, CITO:0.05Sm^{3+}, CITO:0.05Pr^{3+}, and CITO:0.003Mn^{4+} phosphors remained at about 78.70%, 79.54%, 41.75%, and 7.90%, respectively, as shown in Figs. 5(e)–5(h). Markedly, the Ln^{3+}-activated CITO materials have better thermal stability than the TM ions (Mn^{4+}). The activation energies (ΔE) were estimated to be 0.195 eV (CITO:0.4Eu^{3+}), 0.304 eV (CITO:0.05Sm^{3+}), 0.236 eV (CITO:0.05Pr^{3+}), and 0.430 eV (CITO: 0.003Mn^{4+}), as presented in Fig. 5(i). Although some researchers have always believed that the thermal stability of phosphors can be evaluated simply by comparing activation energy, only activation energy cannot sufficiently identify the strength of the thermal quenching based on the previous reports, such as $Na_2CaP_2O_7$:Eu^{3+} (90.63% at 423 K, ΔE = 0.26 eV) [53], La_2CaSnO_6:Eu^{3+} (70.94% at 423 K, ΔE = 0.232 eV) [54], $Ca_4ZrGe_3O_{12}$:Cr^{3+} (69% at 373 K, ΔE = 0.38 eV) [55], $Ca_2LaHf_2Al_3O_{12}$:Eu^{3+} (73.7% at 423 K, ΔE = 0.373 eV) [56], $CaGd_2HfSc(AlO_4)_3$:Ce^{3+} (27% at 423 K, ΔE = 0.29 eV) [57], Ca_2LaSbO_6:Sm^{3+} (59.04% at 423 K, ΔE = 0.2689 eV) [58], and Sr_2InSbO_6:Sm^{3+} (5.8% at 523 K, ΔE = 0.32 eV) phosphors [59]. Thus, the directly effective method for better investigating the thermal stability is to compare temperature-dependent emission intensity.

As identified above, the CITO:Eu^{3+} phosphors with ultra-high internal PLQYs and good thermal stability could be suggested for solid-state lighting. As a result, the white LED devices based on the ~385 and ~405 nm chips were packaged. Eelectroluminescence (EL) emission spectra of the fabricated white LED devices under different forward currents are recorded in Figs. 6(a) and 6(b). Furthermore, the corresponding chromaticity coordinates and CRI and CCT values are listed in Table 3. Clearly, the white LED devices based on the ~405 nm chip exhibited more excellent

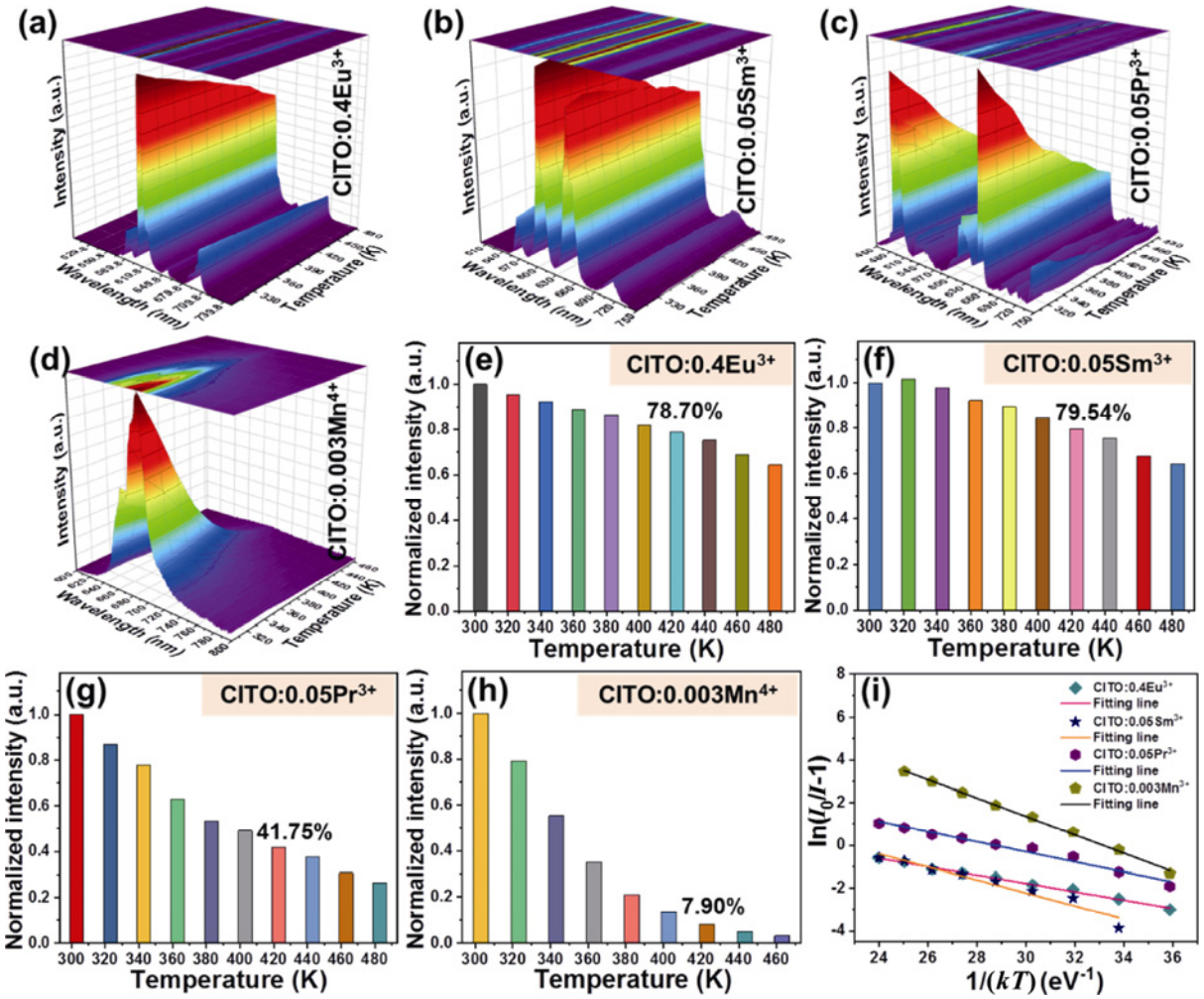

Fig. 5 3D and 2D fluorescence topographical mappings and normalized emission intensity values of (a, e) CITO:0.4Eu^{3+}, (b, f) CITO:0.05Sm^{3+}, (c, g) CITO:0.05Pr^{3+}, and (d, h) CITO:0.003Mn^{4+} phosphors. (i) Plot of $1/(kT)$ vs. $\ln(I_0/I - 1)$ of the prepared phosphors.

performance (i.e., CRI > 89 and CCT < 4900 K). Particularly, it showed a high CRI value (91.51) under a forward current of 10 mA, which is more excellent than the white LED device based on the ~385 nm chip (the optimal CCT and CRI values were 5757 K and 83.26, respectively), indicating that the white LED device based on the ~405 nm chip is more suitable for indoor illumination. The reasons why the white LED devices based on the different LED chips (~385 and ~405 nm) showed different CRI and CCT values could be explained based on the following aspects. Firstly, the emission intensity of the packaged phosphors including the obtained sample and commercial one was different under different λ_{ex}; obviously, the relative emission intensity of the BSS:Eu^{2+} was much stronger than that of BAM:Eu^{2+} commercial phosphors at the ~405 nm LED chip with respect to the excitation of the ~385 nm LED chip. Secondly, although the encapsulation (packaged LED) steps are the same, it is still hard to guarantee the same content of powder slurry on each LED device. Thirdly, these two different LED chips (~385 and 405 nm) emit distinct emission intensity. Besides, the packaged white LED device also exhibited different CRI and CCT values under various forward currents. It is known to all of us that the operating temperature will raise at a high-power (high-forward-current) condition. As such, it implies that these phosphors have different thermal stability resulting in distinct contributions (CCT and CRI) of the emission spectra of the white LED devices. On the other hand, these packaged white LED devices emitted dazzling white light under a low forward current of 10 mA, as shown in Fig. 6(c), further demonstrating that the CITO:Eu^{3+} phosphors can be applied in solid-state lighting as a kind of red-emitting materials with an excellent QY.

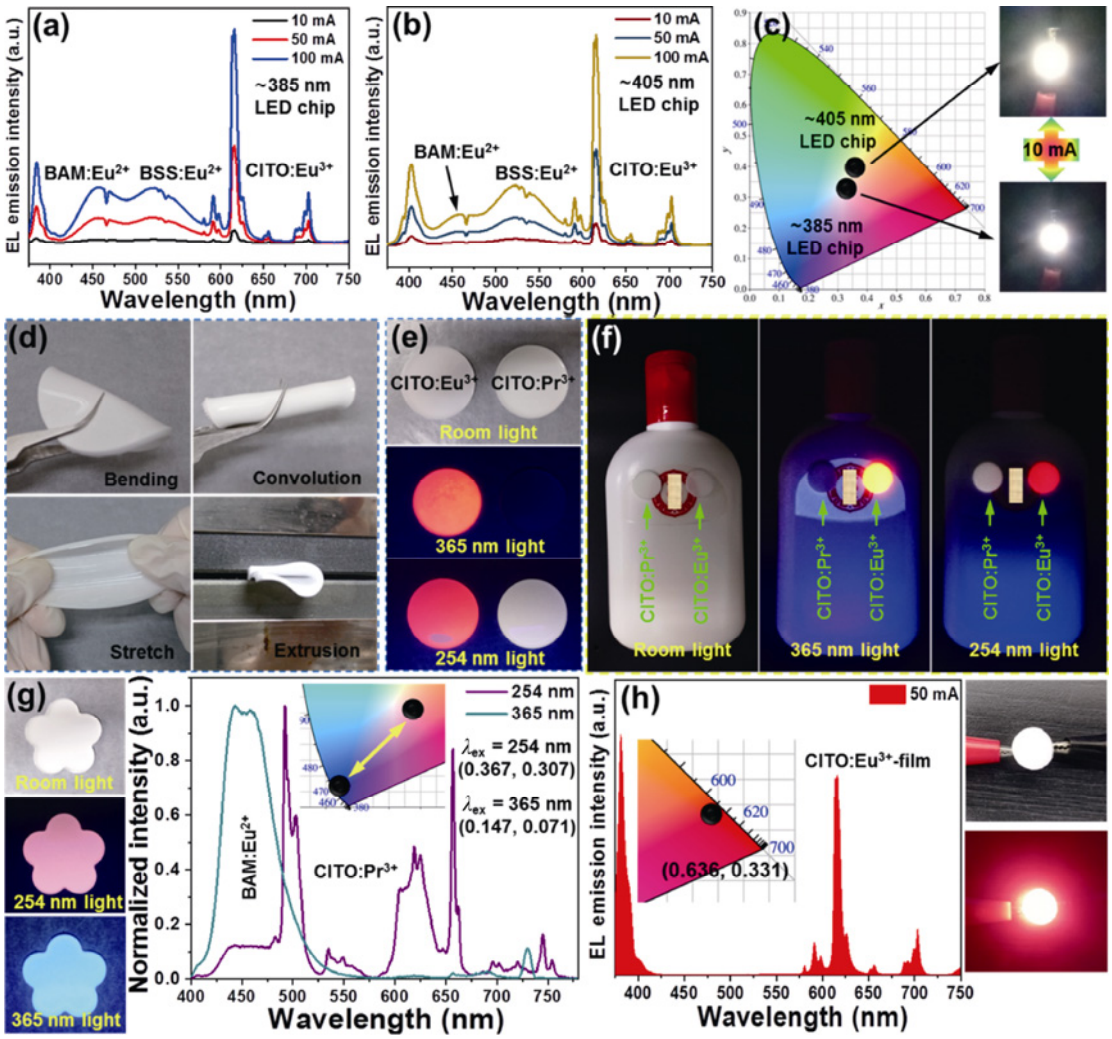

Fig. 6 Packaged white LED devices based on (a) ~385 nm chip and (b) ~405 nm chip under various forward currents of 10, 50, and 100 mA. (c) CIE chromaticity diagram and working graphics of white LED devices under a forward current of 10 mA. (d) Multi-state displays of CITO:Eu^{3+} phosphor-converted film. (e) CITO:Eu^{3+} and CITO:Pr^{3+} phosphor-converted films under room light, 365 nm light, and 254 nm light. (f) Potential application in the product. (g) CITO:Pr^{3+}–BAM:Eu^{2+} film and its normalized emission spectra under 254 and 365 nm excitation. The inset of (g) shows the corresponding CIE chromaticity coordinates. (h) EL emission spectrum of red-emission LED device based on CITO:Eu^{3+} phosphor-converted film under a forward current of 50 mA. The inset of (h) shows the corresponding CIE chromaticity coordinate.

Table 3 Relative parameters of packaged white LED devices

White LED	Current (mA)	Chromaticity coordinate	CRI	CCT (K)
~385 nm chip	10	(0.3267, 0.3422)	83.26	5757
	50	(0.3263, 0.3358)	80.59	5784
	100	(0.3257, 0.3314)	78.87	5819
~405 nm chip	10	(0.3532, 0.3984)	91.51	4886
	50	(0.3541, 0.3918)	90.32	4836
	100	(0.3544, 0.3891)	89.78	4819

To extend the potential applications of the phosphors, the flexible CITO:Eu^{3+} and CITO:Pr^{3+} phosphor-converted films were fabricated for the application in anti-counterfeiting fields. The flexibility was confirmed via operations of bending, convolution, stretching, and extrusion, as shown in Fig. 6(d). Under different excitation lights (e.g., room light, 254 nm light, and 365 nm light), the CITO:Eu^{3+} and CITO:Pr^{3+} phosphor-converted films emitted different colors originating from their unique emissions, as displayed in Fig. 6(e). With regard to this, it is reasonable to think that this technique has certain anti-counterfeiting ability by combining the CITO:Eu^{3+} and CITO:Pr^{3+} phosphor-converted films, as presented in Fig. 6(f). To further improve the security level, the CITO:Pr^{3+}–BAM:Eu^{2+} film was made in the shape of a flower. Under the room light, 254 nm light, and 365 nm light, the CITO:Pr^{3+}–BAM:Eu^{2+} film displayed white, pink, and

blue emissions, respectively. That is because the CITO:Pr^{3+} and BAM:Eu^{2+} phosphors have different λ_{ex}. Under the 254 nm excitation, the CITO:Pr^{3+}–BAM:Eu^{2+} film emitted clearly featured emission of the CITO:Pr^{3+} and partial emission of the BAM:Eu^{2+} in the chromaticity coordinate of (0.367, 0.307). However, this film illustrated the pure emission of the BAM:Eu^{2+} phosphors with the chromaticity coordinate of (0.147, 0.071) under the 365 nm excitation, as shown in Fig. 6(g). As such, single phosphor-converted films with a special shape can emit three different colors, which greatly improves the security level. Besides, a novel LED structure based on the phosphor-converted film was packaged. This phosphor-converted film structure can have the advantage of environmental-friendly performance in terms of good recyclability. Under a forward current of 50 mA, the red-emitting LED device exhibited a dazzling red emission with the featured emission peaks of the CITO:Eu^{3+} phosphors, while the chromaticity coordinate was determined to be (0.636, 0.331), as shown in Fig. 6(h).

As we mentioned above, the Ln^{3+}/Mn^{4+} co-activated phosphors have been proposed for the use in LIR thermometry. In the CITO lattice, Ln^{3+} and Mn^{4+} have significantly different thermal quenching, which means that the Ln^{3+}/Mn^{4+} co-doped CITO phosphors might obtain excellent sensing properties as a novel candidate in optical thermometry. In this respect, the CITO: 0.4Eu^{3+}/0.003Mn^{4+}, CITO:0.05Sm^{3+}/0.003Mn^{4+}, and CITO:0.05Pr^{3+}/0.003Mn^{4+} phosphors were prepared. To better investigate the Ln^{3+}/Mn^{4+} co-doped CITO phosphors, the suitable λ_{ex} should be figured out first. The normalized PLE spectra of the single-doped samples were presented, and some potential λ_{ex} (e.g., intersection and strongest line) were marked, as shown in Figs. 7(a)–7(c). Afterward, the PL emission spectra of the CITO:0.4Eu^{3+}/0.003Mn^{4+} were recorded under the various λ_{ex} of 299, 373, and 396 nm, as displayed

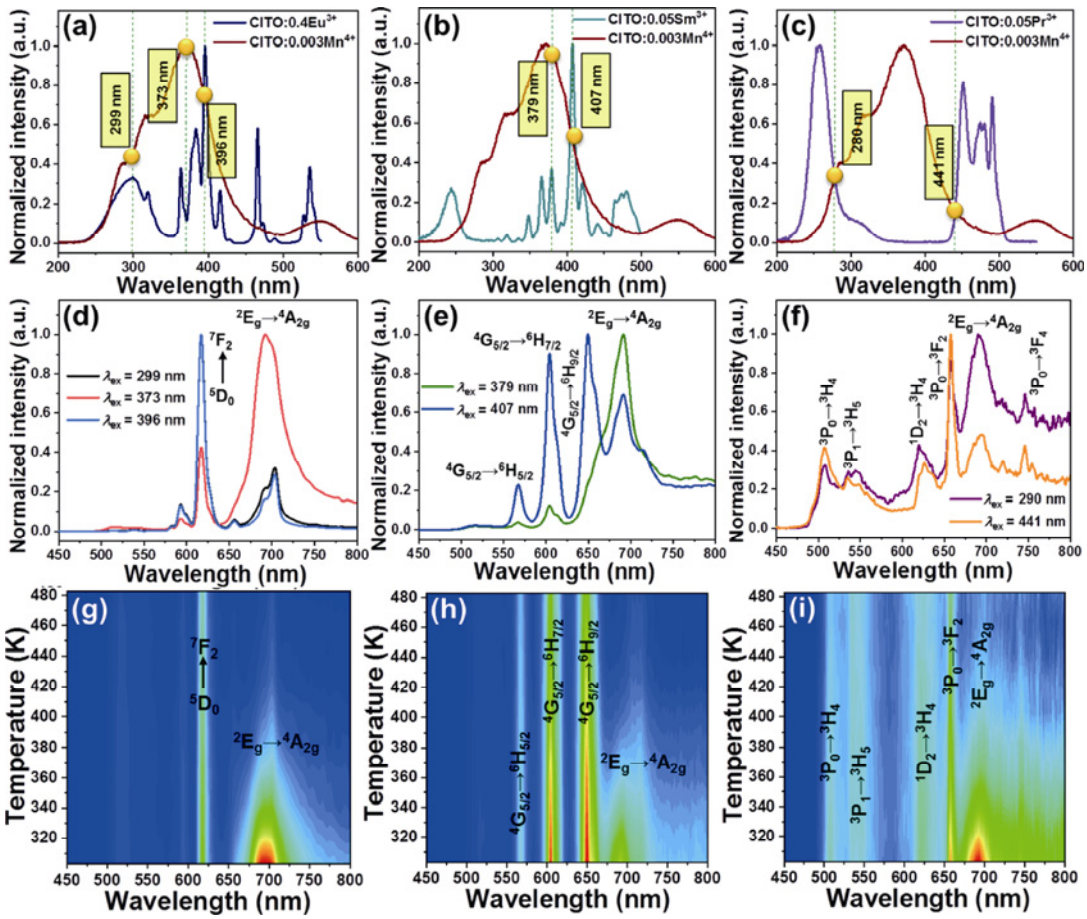

Fig. 7 Normalized PLE spectra of (a) CITO:0.4Eu^{3+}–CITO:0.003Mn^{4+}, (b) CITO:0.05Sm^{3+}–CITO:0.003Mn^{4+}, and (c) CITO:0.05Pr^{3+}–CITO:0.003Mn^{4+} phosphors. Normalized PL emission spectra of (d) CITO:0.4Eu^{3+}/0.003Mn^{4+}, (e) CITO:0.05Sm^{3+}/0.003Mn^{4+}, and (f) CITO:0.05Pr^{3+}/0.003Mn^{4+} phosphors under different λ_{ex}. 2D fluorescence topographical mappings of (g) CITO:0.4Eu^{3+}/0.003Mn^{4+} (λ_{ex} = 373 nm), (h) CITO:0.05Sm^{3+}/0.003Mn^{4+} (λ_{ex} = 407 nm), and (i) CITO:0.05Pr^{3+}/0.003Mn^{4+} (λ_{ex} = 290 nm) phosphors in temperature range of 303–483 K.

in Fig. 7(d). The $^2E_g \rightarrow {}^4A_{2g}$ peak of the Mn^{4+} ion partially overlapped with the $^5D_0 \rightarrow {}^7F_4$ (Eu^{3+}) emission peak. Under λ_{ex} = 299 and 396 nm, it is not clear to distinguish the characteristic emission peaks of the Eu^{3+} and Mn^{4+} ions. However, such issue can be resolved after changing λ_{ex} to 373 nm. With regard to this, the suitable λ_{ex} of the CITO:0.05Sm^{3+}/0.003Mn^{4+} and CITO:0.05Pr^{3+}/0.003Mn^{4+} phosphors were determined to be 407 and 290 nm, respectively, as illustrated in Figs. 7(e) and 7(f), respectively. The 2D fluorescence topographical mappings in the temperature range of 303–483 K are presented in Figs. 7(g)–7(i). Evidently, the various transitions of the Ln^{3+} and Mn^{4+} ions have different thermal quenching in CITO lattices, as shown in Figs. 8(a)–8(h). This might be mainly due to two aspects: One reason is the different occupancy environment (e.g., site, bond length, and *t*), resulting in different structure rigidity; the other one is the different heat resistance of the luminescence activators performing unequal strength of thermal quenching. Besides, the emission region was transferred from dark to light color as the temperature increased, as shown in Fig. 8(i). Particularly, the chromaticity coordinate of the CITO:0.4Eu^{3+}/0.003Mn^{4+} phosphor was (0.555, 0.422) at 303 K and turned to (0.519, 0.459) at 483 K. As for the CITO:0.05Sm^{3+}/0.003Mn^{4+} phosphor, the chromaticity coordinate shifted from (0.593, 0.399) at 303 K to (0.566, 0.422) at 483 K. The chromaticity coordinates of the CITO:0.05Pr^{3+}/0.003Mn^{4+} phosphor were (0.467, 0.498) at 303 K and (0.451, 0.510) at 483 K. These results further demonstrated that the Mn^{4+} ion has more poor thermal stability than the Ln^{3+} ions in the CITO host and fully verified the LIR reasonableness.

The temperature-dependent LIR values of dual-emission

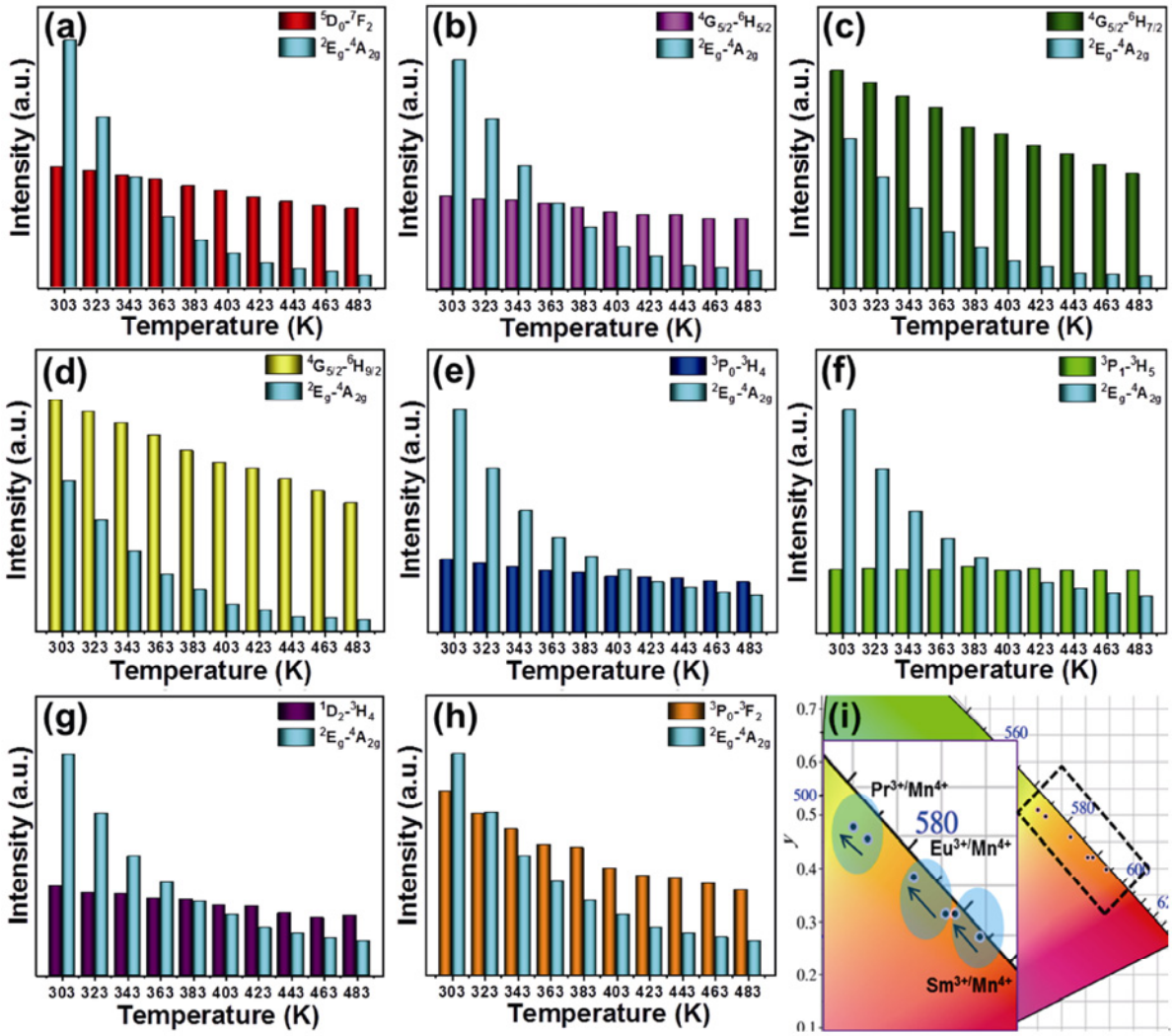

Fig. 8 (a–h) Emission intensity values of various 4f transitions and $^2E_g \rightarrow {}^4A_{2g}$. (i) CIE chromaticity coordinates of co-doped samples at 303 and 483 K.

centers could be defined as [60]:

$$\mathrm{LIR}=\frac{I_{\mathrm{Ln}}}{I_{\mathrm{Mn}}}=\frac{\dfrac{I_{\mathrm{Ln}_0}}{1+A_{\mathrm{Ln}}\exp\left(-\dfrac{E_{\mathrm{Ln}}}{kT}\right)}}{\dfrac{I_{\mathrm{Mn}_0}}{1+A_{\mathrm{Mn}}\exp\left(-\dfrac{E_{\mathrm{Mn}}}{kT}\right)}} \tag{14}$$

In Eq. (14), the luminescence emission intensity at 0 K (I_{Ln0} and I_{Mn0}) should be investigated. Thus, Eq. (14) is not a suitable model to estimate the LIR values in a certain temperature range. Fortunately, Eq. (14) can be written as Eq. (15) by Arrhenius form in a certain temperature range (e.g., 303–483 K) based on Taylor expansion method.

$$\begin{aligned}\mathrm{LIR}&=\frac{I_{\mathrm{Ln}}}{I_{\mathrm{Mn}}}=\frac{1+A_{\mathrm{Mn}}\exp(-\Delta E_{\mathrm{Mn}}/(kT))}{1+A_{\mathrm{Ln}}\exp(-\Delta E_{\mathrm{Ln}}/(kT))}\\&\approx B_1+C_1\exp(-\Delta E/(kT))\end{aligned} \tag{15}$$

As shown in Figs. 9(a)–9(h), the LIR values between the Ln^{3+} transitions and $^2E_g \rightarrow {}^4A_{2g}$ (Mn^{4+}) in the temperature range of 303–483 K were well fitted (Adj. $R^2 > 0.95$) to Eq. (15).

LIR values in CITO:0.4Eu^{3+}/0.003Mn^{4+} phosphor:

$$\mathrm{LIR}_1=\frac{I_{^5\mathrm{D}_0\rightarrow{}^7\mathrm{F}_2}}{I_{^2\mathrm{E}_g\rightarrow{}^4\mathrm{A}_{2g}}}\approx 366.34\exp(-1919.92/T)-0.26 \tag{16}$$

LIR values in CITO:0.05Sm^{3+}/0.003Mn^{4+} phosphor:

$$\mathrm{LIR}_2=\frac{I_{^4\mathrm{G}_{5/2}\rightarrow{}^6\mathrm{H}_{5/2}}}{I_{^2\mathrm{E}_g\rightarrow{}^4\mathrm{A}_{2g}}}\approx 165.7\exp(-1758.41/T)-0.21 \tag{17}$$

$$\mathrm{LIR}_3=\frac{I_{^4\mathrm{G}_{5/2}\rightarrow{}^6\mathrm{H}_{7/2}}}{I_{^2\mathrm{E}_g\rightarrow{}^4\mathrm{A}_{2g}}}\approx 167.7\exp(-1271.57/T)-1.47 \tag{18}$$

$$\mathrm{LIR}_4=\frac{I_{^4\mathrm{G}_{5/2}\rightarrow{}^6\mathrm{H}_{9/2}}}{I_{^2\mathrm{E}_g\rightarrow{}^4\mathrm{A}_{2g}}}\approx 185.8\exp(-1256.34/T)-1.88 \tag{19}$$

LIR values in CITO:0.05Pr^{3+}/0.003Mn^{4+} phosphor:

$$\mathrm{LIR}_5=\frac{I_{^3\mathrm{P}_0\rightarrow{}^3\mathrm{H}_4}}{I_{^2\mathrm{E}_g\rightarrow{}^4\mathrm{A}_{2g}}}\approx 8.75\exp(-739.39/T)-0.45 \tag{20}$$

$$\mathrm{LIR}_6=\frac{I_{^3\mathrm{P}_1\rightarrow{}^3\mathrm{H}_5}}{I_{^2\mathrm{E}_g\rightarrow{}^4\mathrm{A}_{2g}}}\approx 17.32\exp(-1014.9/T)-0.36 \tag{21}$$

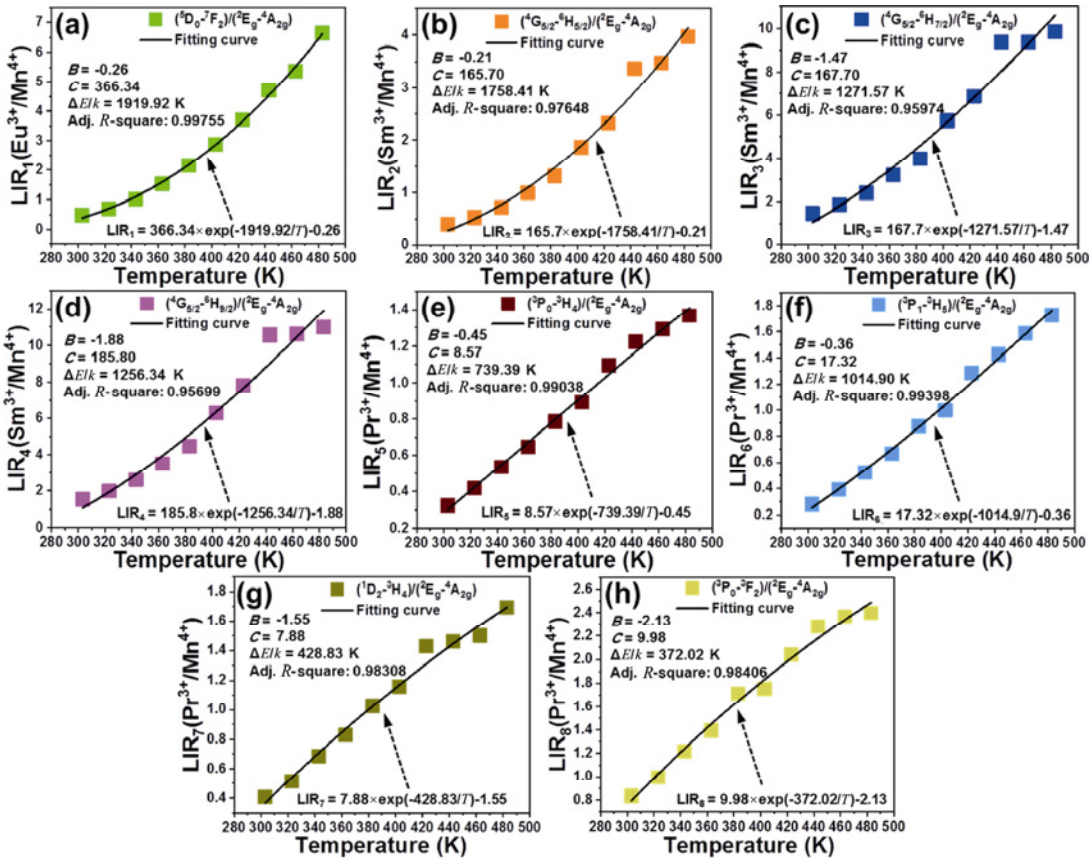

Fig. 9 LIR values of (a) CITO:0.4Eu^{3+}/0.003Mn^{4+}, (b–d) CITO:0.05Sm^{3+}/0.003Mn^{4+}, and (e–h) CITO:0.05Pr^{3+}/0.003Mn^{4+} phosphors between RE ions and Mn^{4+} transitions.

$$\mathrm{LIR}_7 = \frac{I_{^1\mathrm{D}_2\rightarrow{}^3\mathrm{H}_4}}{I_{^2\mathrm{E}_g\rightarrow{}^4\mathrm{A}_{2g}}} \approx 7.88\exp(-428.83/T) - 1.55 \quad (22)$$

$$\mathrm{LIR}_8 = \frac{I_{^3\mathrm{P}_0\rightarrow{}^3\mathrm{F}_2}}{I_{^2\mathrm{E}_g\rightarrow{}^4\mathrm{A}_{2g}}} \approx 9.98\exp(-372.02/T) - 2.13 \quad (23)$$

Hereafter, the absolute sensitivity (S_a) and relative sensitivity (S_r) were estimated to better evaluate sensing performance [60].

$$S_a = \left|\frac{\partial \mathrm{LIR}}{\partial T}\right| = C_1\exp(-\Delta E/(kT)) \times \frac{\Delta E}{kT^2} \quad (24)$$

$$S_r = 100\%\left|\frac{\partial \mathrm{LIR}}{\mathrm{LIR}\partial T}\right| = \frac{100\%C_1\exp\left(\frac{-\Delta E}{kT}\right)}{B_1 + C_1\exp\left(\frac{-\Delta E}{kT}\right)} \times \frac{\Delta E}{kT^2} \quad (25)$$

Based on Eq. (24), the maximum S_a of the LIR_1, LIR_2, LIR_3, LIR_4, LIR_5, LIR_6, LIR_7, and LIR_8 were estimated to be about 0.0566 K^{-1}@483 K, 0.0328 K^{-1}@483 K, 0.0657 K^{-1}@483 K, 0.0741 K^{-1}@483 K, 0.0063 K^{-1}@383 K, 0.0092 K^{-1}@483 K, 0.0089 K^{-1}@303 K, and 0.0119 K^{-1}@303 K, respectively, as shown in Fig. 10(a). Moreover, the relative sensing sensitivity can intuitively express the sensing performance relative to S_a. The S_r was analyzed with the help of Eq. (25). Note that S_r exhibited a downward tendency, as displayed in Fig. 10(b). Interestingly, the optimal S_r value of the CITO:0.4Eu^{3+}/0.003Mn^{4+} phosphor (LIR_1) was as high as 3.49 %·K^{-1}. As for the CITO:0.05Sm^{3+}/ 0.003Mn^{4+} phosphor, the S_r values were estimated to be about 3.30 %·K^{-1} (LIR_2), 3.32 %·K^{-1} (LIR_3), and 3.80 %·K^{-1} (LIR_4). Eventually, the S_r values of the CITO:0.05Pr^{3+}/0.003Mn^{4+} phosphor were determined to be about 2.03 %·K^{-1} (LIR_5), 2.71 %·K^{-1} (LIR_6), 2.46 %·K^{-1} (LIR_7), and 1.49 %·K^{-1} (LIR_8). It is clear that the transition peaks and doping ions affect S_r. Particularly, the CITO:0.05Sm^{3+}/0.003Mn^{4+} phosphor exhibited the more excellent S_r (3.80 %·K^{-1} (LIR_4)) than those of the other Ln^{3+}/Mn^{4+} co-doped samples. On the other hand, these S_r are higher than those of some previous LIR thermometry, such as $YNbO_4$:Pr^{3+}/ Tb^{3+} (1.01 %·K^{-1}) [61], $(Ba,Sr)_3Lu_4O_9$:Er^{3+}/Yb^{3+} (0.88 %·K^{-1}) [62], $ZnAl_2O_4$:Cr^{3+}/Mn^{2+} (3 %·K^{-1}) [63], $Ba_2TiGe_2O_8$:

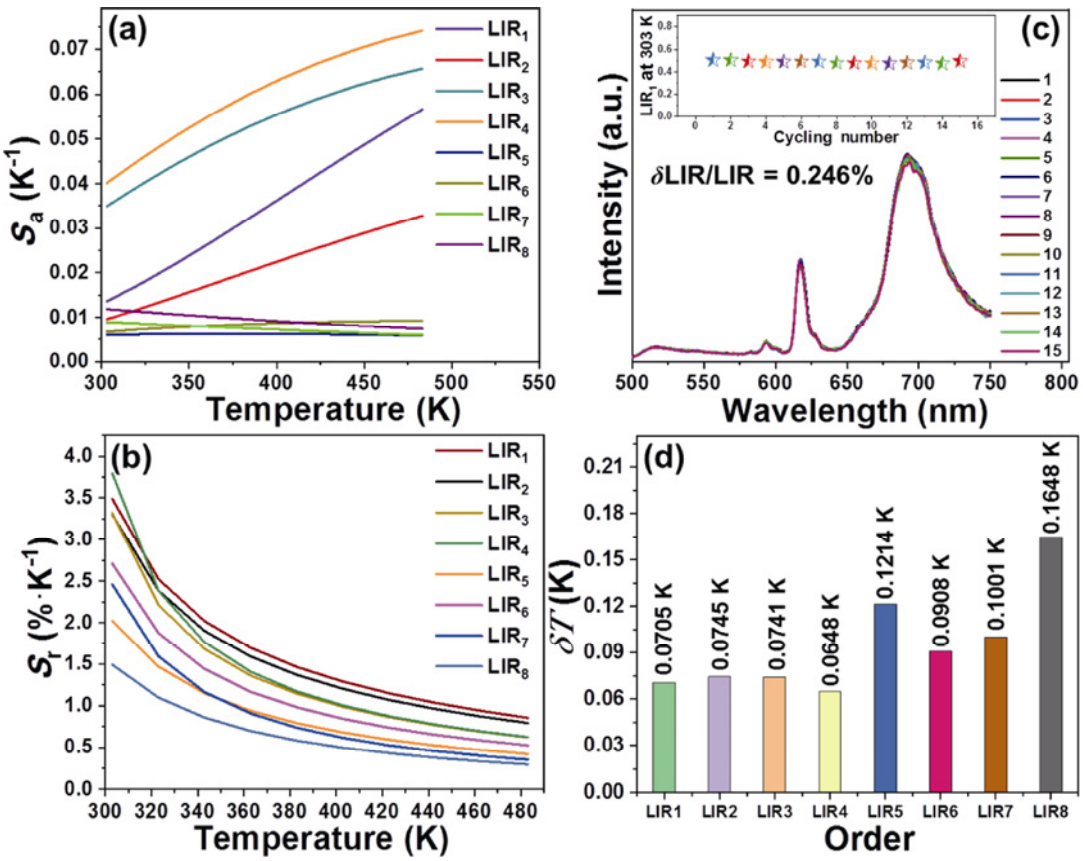

Fig. 10 (a) S_a and (b) S_r of the prepared samples. (c) Cycling measurements of CITO:0.4Eu^{3+}/0.003Mn^{4+} phosphor at 303 K. (d) Temperature resolution (δT) of LIR thermometry.

$Yb^{3+}/Ho^{3+}/Er^{3+}$ (0.716 %·K^{-1}) [64], and $BaAl_{12}O_{19}$:$Sm^{2+}/SrAl_{12}O_{19}$:Sm^{3+} (2.47 %·K^{-1}) phosphors [65]. It is suggested that the Ln^{3+}/Mn^{4+} co-doped CITO phosphors with good relative sensing sensitivity could be potential for optical temperature sensors. The δT can be calculated by Eq. (26):

$$\delta T = \frac{\delta \mathrm{LIR}}{S_r \mathrm{LIR}} \tag{26}$$

where δLIR/LIR is the experimental relative error depending on the instrument. Thus, the cycling measurements (15 times) at 303 K of the CITO: $0.4Eu^{3+}/0.003Mn^{4+}$ phosphor were tested, as shown in Fig. 10(c). The δLIR/LIR was calculated to be 0.246%. Figure 10(d) shows δT of the LIR_1 (0.0705 K), LIR_2 (0.0745 K), LIR_3 (0.0741 K), LIR_4 (0.0648 K), LIR_5 (0.1214 K), LIR_6 (0.0908 K), LIR_7 (0.1001 K), and LIR_8 (0.01648 K). Such observation suggested that the Ln^{3+}/Mn^{4+} co-doped CITO phosphors with beneficial δT could be applied in high-sensing-sensitivity luminescence thermometry.

4 Conclusions

In summary, this work systematically analyzed the crystal structures and optical properties of the luminescent activators (Eu^{3+}, Sm^{3+}, Pr^{3+}, and Mn^{4+}) single-/co-doped CITO phosphors. Due to some remarkable optical performance, e.g., ultra-high internal PLQY (89.1%) and good thermal stability (78.70% at 423 K) and color purity (94.85%), the strongly red-emitting CITO:$0.4Eu^{3+}$ phosphor was determined to become a potential candidate for the white LED devices. Moreover, the correspondingly packaged LED device showed an excellent CRI value (91.51) and a beneficial CCT value (4886 K) for indoor illumination. On the other hand, the CITO:Pr^{3+}–BAM:Eu^{2+} film with elastic deformation as well as the CITO:Eu^{3+} and CITO:Pr^{3+} phosphor-converted films was fabricated for the anti-counterfeiting field because they can emit different colors under various λ_{ex}. Tailoring their special characters or shapes can easily improve the security levels, and its stable construction guarantees long service life even in harsh environment. Besides, it was also verified that the novel LED structure based on the CITO:Eu^{3+} film emitted a dazzling red emission. Eventually, owing to distinct thermal quenching between the Ln^{3+} and Mn^{4+} ions, the LIR thermometry based on the various 4f (Ln^{3+}) and $^2E_g \rightarrow {}^4A_{2g}$ (Mn^{4+}) transitions was analyzed. Especially, the CITO:$0.05Sm^{3+}/0.003Mn^{4+}$ phosphor exhibited higher S_r (3.80 %·K^{-1}) compared to the CITO:$0.05Pr^{3+}/0.003Mn^{4+}$ and CITO: $0.4Eu^{3+}/0.003Mn^{4+}$ phosphors. Consequently, for the advanced CITO:Ln^{3+}/Mn^{4+} phosphors, the obtained results can provide a deep insight into multifunctional optical platforms such as solid-state lighting, flexible anti-counterfeiting films, and LIR thermometry.

Acknowledgements

This work was supported by the National Research Foundation of Korea (NRF) grant funded by the Korean government (MSIP) (No. 2018R1A6A1A03025708).

Electronic Supplementary Material

Supplementary material is available in the online version of this article at https://doi.org/10.26599/JAC.2023.9220731.

References

[1] Cai YF, Yang YF, Liu HX, *et al*. Synthesis of the red-emitting $(Ba,Ca)_2ScAlO_5:Eu^{3+}$ phosphors with photoluminescence properties. *Inorg Chem* 2022, **61**: 8529–8539.

[2] Hua YB, Wang T, Yu JS, *et al*. Modulating A site compositions of europium(III)-doped double-perovskite niobate phosphors. *Inorg Chem Front* 2022, **9**: 6211–6224.

[3] Leng ZH, Bai H, Qing Q, *et al*. A zero-thermal-quenching blue phosphor for sustainable and human-centric WLED lighting. *ACS Sustainable Chem Eng* 2022, **10**: 10966–10977.

[4] Ye SS, Ding JY, Wu QS. MMCT-induced high-bright yellow light-emitting phosphor Bi^{3+}-activated Ba_2YGaO_5 used for WLED. *Chem Eng J* 2022, **428**: 131238.

[5] Kang Y, Li SX, Tian RD, *et al*. Fine-grained phosphors for red-emitting mini-LEDs with high efficiency and super-luminance. *J Adv Ceram* 2022, **11**: 1383–1390.

[6] Liu X, Qian XL, Zheng P, *et al*. Composition and structure design of three-layered composite phosphors for high color rendering chip-on-board light-emitting diode devices. *J Adv Ceram* 2021, **10**: 729–740.

[7] Peng Y, Yu ZK, Zhao JZ, *et al*. Unique sandwich design of high-efficiency heat-conducting phosphor-in-glass film for high-quality laser-driven white lighting. *J Adv Ceram* 2022, **11**: 1889–1900.

[8] Peng Y, Wang H, Liu JX, *et al*. Broad-band and stable phosphor-in-glass enabling ultrahigh color rendering for all-inorganic high-power WLEDs. *ACS Appl Electron Mater* 2020, **2**: 2929–2936.

[9] Zhao M, Liao HX, Molokeev MS, *et al*. Emerging ultra-narrow-band cyan-emitting phosphor for white LEDs with enhanced color rendition. *Light-Sci Appl* 2019, **8**: 38.

[10] Dang PP, Li GG, Yun XH, *et al*. Thermally stable and

highly efficient red-emitting Eu^{3+}-doped $Cs_3GdGe_3O_9$ phosphors for WLEDs: Non-concentration quenching and negative thermal expansion. *Light-Sci Appl* 2021, **10**: 29.

[11] Zhang Q, Wang XC, Ding X, *et al*. A potential red-emitting phosphor $BaZrGe_3O_9:Eu^{3+}$ for WLED and FED applications: Synthesis, structure, and luminescence properties. *Inorg Chem* 2017, **56**: 6990–6998.

[12] Khan SU, Khan WU, Khan WU, *et al*. Eu^{3+},Sm^{3+} deep-red phosphors as novel materials for white light-emitting diodes and simultaneous performance enhancement of organic–inorganic perovskite solar cells. *Small* 2020, **16**: 2001551.

[13] Geng X, Xie Y, Chen SS, *et al*. Enhanced local symmetry achieved zero-thermal-quenching luminescence characteristic in the $Ca_2InSbO_6:Sm^{3+}$ phosphors for w-LEDs. *Chem Eng J* 2021, **410**: 128396.

[14] Li GX, Shi XY, Lu XY, *et al*. Local structure modulation-induced highly efficient red-emitting $Ba_2Gd_{1-x}Y_xNbO_6:Mn^{4+}$ phosphors for warm WLEDs. *Inorg Chem* 2021, **60**: 17398–17406.

[15] Zhou JB, Chen YY, Jiang CY, *et al*. High moisture resistance of an efficient Mn^{4+}-activated red phosphor $Cs_2NbOF_5:Mn^{4+}$ for WLEDs. *Chem Eng J* 2021, **405**: 126678.

[16] Zhou YY, Ming H, Zhang S, *et al*. Unveiling Mn^{4+} substitution in oxyfluoride phosphor $Rb_2MoO_2F_4:Mn^{4+}$ applied to wide-gamut fast-response backlight displays. *Chem Eng J* 2021, **415**: 128974.

[17] Hua YB, Seo YU, Kim SY, *et al*. Rare-earth-free $Sr_2YSb_{1-x}O_6:xMn^{4+}$: Synthesis, structure, luminescence behavior, thermal stability, and applications. *Chem Eng J* 2021, **412**: 128633.

[18] Zhang WH, Lv P, Li YJ, *et al*. Efficient hole extraction with Eu^{3+}-doped $CsPbBr_3$ QD interface modification for HTL-free $CH_3NH_3PbI_3$:Na perovskite solar cells. *Sol Energy* 2022, **245**: 224–230.

[19] Demirdogen RE, Emen FM, Karaçolak AI, *et al*. Preparation of novel $CaMoO_4:Eu^{3+}$–MCM-41 nanocomposites and their applications and monitoring as drug release systems. *J Drug Deliv Sci Tec* 2021, **66**: 102792.

[20] Liu XM, Lin J. $LaGaO_3$:A (A = Sm^{3+} and/or Tb^{3+}) as promising phosphors for field emission displays. *J Mater Chem* 2008, **18**: 221–228.

[21] Abdel Wahab EA, El-Maaref AA, Shaaban KS, *et al*. Lithium cadmium phosphate glasses doped Sm^{3+} as a host material for near-IR laser applications. *Opt Mater* 2021, **111**: 110638.

[22] Tanaka H, Kalusniak S, Badtke M, *et al*. Visible solid-state lasers based on Pr^{3+} and Tb^{3+}. *Prog Quant Electron* 2022, **84**: 100411.

[23] Hua Y, Wang T, Xia W, *et al*. Constructing novel red-emitting $Ba_2Y_{0.8}Eu_{0.2}NbO_6:Mn^{4+}$ phosphors for multi-type luminescent thermometers and high-security anti-counterfeiting films. *Mater Today Chem* 2022, **23**: 100710.

[24] Zang ZH, Liu L, Yang L, *et al*. Preparation and performance of Eu^{3+}-doped $BaSnF_4$-based solid-state electrolytes for room-temperature fluoride-ion batteries. *ACS Sustainable Chem Eng* 2021, **9**: 12978–12989.

[25] Tian XY, Li JL, Sheng HY, *et al*. Luminescence and optical thermometry based on silico–carnotite $Ca_3Y_2Si_3O_{12}:Pr^{3+}$ phosphor. *Ceram Int* 2022, **48**: 3860–3868.

[26] Hua YB, Li H, Wang T, *et al*. Customization of novel double-perovskite $(Ca,Sr)_2InNbO_6:Mn^{4+}$ red-emitting phosphors for luminescence lifetime thermometers with good relative sensing sensitivity. *J Alloys Compd* 2022, **925**: 166498.

[27] Yun XY, Zhou J, Zhu YH, *et al*. A potentially multifunctional double-perovskite $Sr_2ScTaO_6:Mn^{4+}$,Eu^{3+} phosphor for optical temperature sensing and indoor plant growth lighting. *J Lumin* 2022, **244**: 118724.

[28] Liao JS, Wang MH, Kong LY, *et al*. Dual-mode optical temperature sensing behavior of double-perovskite $CaGdMgSbO_6$: Mn^{4+}/Sm^{3+} phosphors. *J Lumin* 2020, **226**: 117492.

[29] Wang MH, Han Z, Huang JX, *et al*. $NaLaMgWO_6:Mn^{4+}/Pr^{3+}/Bi^{3+}$ bifunctional phosphors for optical thermometer and plant growth illumination matching phytochrome PR and PFR. *Spectrochim Acta A* 2021, **259**: 119915.

[30] Zheng T, Luo LH, Du P, *et al*. Highly-efficient double perovskite Mn^{4+}-activated Gd_2ZnTiO_6 phosphors: A bifunctional optical sensing platform for luminescence thermometry and manometry. *Chem Eng J* 2022, **446**: 136839.

[31] Rajkumar G, Ponnusamy V, Kanmani GV, *et al*. Ternary type $BaY_2ZnO_5:Eu^{3+}$ deep-red phosphor for possible latent fingerprint, security ink and WLED applications. *Ceram Int* 2022, **48**: 10–21.

[32] Shi W, Chen JX, Kong JY, *et al*. A novel highly thermal-stable red-emitting $CaGdSbWO_8:Eu^{3+}$ phosphor with scheelite structure for high CRI w-LEDs, security ink, and latent fingerprint. *J Alloys Compd* 2022, **914**: 165134.

[33] Liu HM, Zhang WY, Liang HW, *et al*. Discovery of a new phosphor via aliovalent cation substitution: DFT predictions, phase transition and luminescence properties for lighting and anti-counterfeiting applications. *J Mater Chem C* 2021, **9**: 1622–1631.

[34] Bao S, Yu HY, Gao GY, *et al*. Rare-earth single atom based luminescent composite nanomaterials: Tunable full-color single phosphor and applications in WLEDs. *Nano Res* 2022, **15**: 3594–3605.

[35] Chen XA, Bian RR, Xiao WQ, *et al*. A new rare-earth oxyborate $Ba_3BiPbEuO(BO_3)_4$ and the luminescence properties of the $Ba_3BiPbY_{1-x}Eu_xO(BO_3)_4$ phosphors. *Dalton Trans* 2022, **51**: 9454–9466.

[36] Wang YF, Ding F, Wu JY, *et al*. Site preference-driven Mn^{4+} stabilization in double perovskite phosphor regulating quantum efficiency from zero to champion. *Inorg Chem* 2022, **61**: 3631–3640.

[37] Zhang L, Xu YH, Yin SW, *et al*. Rare-earth-free Mn^{4+}-doped double perovskite structure phosphor for near ultraviolet excitation of WLED and plant cultivation. *J Alloys Compd* 2022, **891**: 162042.

[38] Han B, Yang X, Ren J, *et al*. Thermally stable deep-red emitting $Sr_2GdTaO_6:Mn^{4+}$ double perovskites for indoor plant growth LEDs. *Mater Today Chem* 2022, **23**: 100737.

[39] Cai YY, Liu SB, Zhao L, *et al*. Delayed stress memory by $CaAl_2O_4:Eu^{2+}$ mechanoluminescent phosphor with defect engineering regulation. *J Adv Ceram* 2022, **11**: 1319–1329.

[40] Guo J, Guo JL, Gao J, *et al*. A novel broadband-excited $LaNb_2VO_9:Sm^{3+}$ orange–red-emitting phosphor with zero-thermal-quenching behavior for WLEDs and personal identification. *Ceram Int* 2022, **48**: 26992–27002.

[41] Xie Y, Geng X, Guo J, *et al*. Luminescence of a novel double-perovskite $Sr_2InSbO_6:Eu^{3+}$ orange–red-emitting phosphor for white LEDs and visualization of latent fingerprints. *Mater Res Bull* 2022, **146**: 111574.

[42] Yu PF, Cui RR, Gong XY, *et al*. Photoluminescence properties of $Ba_3In_2WO_9:Eu^{3+}$: A novel red-emitting phosphor for WLEDs. *J Mater Sci Mater Electron* 2022, **33**: 14882–14893.

[43] Blasse G. Energy transfer between inequivalent Eu^{2+} ions. *J Solid State Chem* 1986, **62**: 207–211.

[44] Reisfeld R, Greenberg E, Velapoldi R. Luminescence quantum efficiency of Gd and Tb in borate glasses and the mechanism of energy transfer between them. *J Chem Phys* 1972, **56**: 1698–1705.

[45] Blasse G. Energy transfer in oxidic phosphors. *Phys Lett A* 1968, **28**: 444–445.

[46] Zhang F, Bi ZF, Huang AP, *et al*. Luminescence and Judd–Ofelt analysis of the Pr^{3+} doped fluorotellurite glass. *J Lumin* 2015, **160**: 85–89.

[47] Suresh C, Darshan GP, Sharma SC, *et al*. Imaging sweat pore structures in latent fingerprints and unclonable anti-counterfeiting patterns by sensitizers blended $LaOF:Pr^{3+}$ nanophosphors. *Opt Mater* 2020, **100**: 109625.

[48] Wang H, Liu XY, Hong F, *et al*. Luminescence properties, crystal field and nephelauxetic effect on $(NH_4)_2NaMF_6:Mn^{4+}$ (M = Al, Ga and In) red phosphors for warm white light-emitting diodes. *J Lumin* 2022, **251**: 119242.

[49] Li GX, Li G, Mao QN, *et al*. Efficient luminescence lifetime thermometry with enhanced Mn^{4+}-activated $BaLaCa_{1-x}Mg_xSbO_6$ red phosphors. *Chem Eng J* 2022, **430**: 132923.

[50] Li ZY, Zhang XH, Wu J, *et al*. A novel inequivalent double-site substituted red phosphor $Li_4AlSbO_6:Mn^{4+}$ with high color purity: Its structure, photoluminescence properties, and application in warm white LEDs. *J Mater Chem C* 2021, **9**: 13236–13246.

[51] Wang YJ, Yu CK, Zhou YY, *et al*. Mn^{4+} doped narrowband red phosphors with short fluorescence lifetime and high color stability for fast-response backlight display application. *J Alloys Compd* 2021, **855**: 157347.

[52] Hua Y, Yu JS. An anti-counterfeiting strategy of polydimethylsiloxane flexible light-emitting films based on non-rare-earth Mn^{4+}-activated Ba_2LaTaO_6 phosphors. *Mater Today Chem* 2022, **26**: 101109.

[53] Meena ML, Som S, Chaurasiya R, *et al*. Spectroscopic, optical properties and ab-initio calculation of thermally stable $Na_2Ca_{1-x}P_2O_7:xEu^{3+}$ phosphors for wLEDs. *Ceram Int* 2022, **48**: 20940–20947.

[54] Xu YY, Li GF, Guan XF, *et al*. Synthesis, crystal structure and photoluminescence properties of novel double perovskite $La_2CaSnO_6:Eu^{3+}$ red-emitting phosphors. *J Rare Earth* 2022, **40**: 1682–1690.

[55] Xiang JM, Zheng JM, Zhao XQ, *et al*. Synthesis of broadband NIR garnet phosphor $Ca_4ZrGe_3O_{12}:Cr^{3+},Yb^{3+}$ for NIR pc-LED applications. *Mater Chem Front* 2022, **6**: 440–449.

[56] Ma N, Li W, Devakumar B, *et al*. Dazzling red-emitting europium(III) ion-doped $Ca_2LaHf_2Al_3O_{12}$ garnet-type phosphor materials with potential application in solid-state white lighting. *Inorg Chem* 2022, **61**: 6898–6909.

[57] Li W, Ma N, Devakumar B, *et al*. Blue-light-excitable broadband yellow-emitting $CaGd_2HfSc(AlO_4)_3:Ce^{3+}$ garnet phosphors for white light-emitting diode devices with improved color rendering index. *Mater Today Chem* 2022, **23**: 100638.

[58] Han BJ, Ren J, Teng PP, *et al*. Synthesis and photoluminescence properties of a novel double perovskite $Ca_2LaSbO_6:Sm^{3+}$ phosphor for w-LEDs. *Ceram Int* 2022, **48**: 971–980.

[59] Xia WD, Li L, Hua YB, *et al*. Realizing dual-mode luminescent thermometry with excellent sensing sensitivity in single-phase samarium (III)-doped antimonite phosphors. *J Alloys Compd* 2022, **917**: 165435.

[60] Gao Y, Huang F, Lin H, *et al*. A novel optical thermometry strategy based on diverse thermal response from two intervalence charge transfer states. *Adv Funct Mater* 2016, **26**: 3139–3145.

[61] Yuan SW, Zhao S, Lou LL, *et al*. Fluorescence intensity ratio optical thermometer $YNbO_4:Pr^{3+},Tb^{3+}$ based on intervalence charge transfer. *Powder Technol* 2022, **395**: 83–92.

[62] Hu JX, Zhang X, Zheng HH, *et al*. Improved photoluminescence and multi-mode optical thermometry of Er^{3+}/Yb^{3+} co-doped $(Ba,Sr)_3Lu_4O_9$ phosphors. *Ceram Int* 2022, **48**: 3051–3058.

[63] Zhu BJ, Ren SQ, Liu YL, *et al*. Influence of Mn^{2+} ions on the structure, spectral characteristics and optical thermometry performances of $ZnAl_2O_4:Cr^{3+}$ multifunctional phosphors. *J Lumin* 2022, **244**: 118736.

[64] Wang ZY, Xu HY, Jia MC, *et al*. Multifunctional lanthanide ions-doped $Ba_2TiGe_2O_8$ phosphor for near-infrared ratiometric thermometer and information security. *J Lumin* 2022, **243**: 118652.

[65] Xu CW, Li CX, Deng DG, *et al*. A dual-mode optical thermometer with high sensitivity based on $BaAl_{12}O_{19}:Sm^{2+}$/$SrAl_{12}O_{19}:Sm^{3+}$ solid solution phosphors. *Inorg Chem* 2022, **61**: 7989–7999.